ABSTRACT

Title of Dissertation:	LAB-ON-A-CHIP INTEGRATION OF SIZE-BASED SEPARATION TECHNIQUES FOR ISOLATION OF BACTERIA FROM BLOOD
	Jung Yeon Han, Ph.D., 2018
Dissertation directed by:	Professor Don L. DeVoe Department of Mechanical Engineering

Clinical sample preparation is an essential process in modern diagnostics for maximizing sensitivity and specificity of detection and for ensuring reliability of assay readout. In general, sample preparation typically involves isolating and concentrating a population of target molecules, cells, or particles together with the removal of undesired components from specimen that could otherwise interfere with target detection. The identification of bacteria from complex clinical matrices such as blood presents a particular sample preparation challenge. Conventional culture-based methods typically require at least 24 h of incubation time, making this approach unsuitable for use in rapid diagnostics. Therefore, the development of sample preparation methods for bacteria with rapid processing time, high purification efficiency, and large volumetric throughput to enable analysis of low bacteria concentrations in blood remains a key challenge.

This dissertation is focused on realizing a universal platform for preparing microbial sample from blood that is free lysis buffer, electric field, or affinity-based capture methods. First, we developed the porous silica monolith elements integrated into thermoplastic devices for isolation of intact bacteria from blood, enabling the application of emerging detection methods that supports bacterial identification from purified cell populations. Second, to support high throughput analysis of blood samples procured in resource-limited environments, microfluidics elements integrated directly into a syringe are demonstrated by utilizing the deterministic lateral displacement technique and the Dean flow focusing methods. Through these approaches blood cell reduction prior to bacteria isolation can be achieved, thereby increasing the overall sample volume that may be processed by the system. Additionally, a miniaturized hydrocylone capable of operating at tens of milliliters per minute feed rate is presented. Complex microstructures successfully realized at a hundred-micron scale by 3D printing technique presented a promising route to the unconventional microfluidic systems. Lastly, we demonstrated ancillary microfluidic components required to enable full operation of the system in a low-cost lab-on-a-chip format suitable for implementation in resource-limited environments and optimize overall operation of the platform to achieve throughput, sensitivity, and selectivity suitable for clinical application when coupling the platform with downstream detection methods designed for assay readout from intact bacteria.

LAB-ON-A-CHIP INTEGRATION OF SIZE-BASED SEPARATION TECHNIQUES FOR ISOLATION OF BACTERIA FROM BLOOD

by

Jung Yeon Han

Dissertation submitted to the Faculty of the Graduate School of the
University of Maryland, College Park, in partial fulfillment
of the requirements for the degree of
Doctor of Philosophy
2018

Advisory Committee:
Professor Don L. DeVoe, University of Maryland, Chair
Professor John Fisher, University of Maryland, Dean's Representative
Professor Srinivasa R. Raghavan, University of Maryland
Professor Panagiotis Dimitrakopoulos, University of Maryland
Professor Kyu Yong Choi, University of Maryland

Dedication

Dedicated to the loving memory of my grandfather Ki Ryong Han,
who was always my greatest supporter.

Acknowledgements

First of all, I would like to express my gratitude to my adviser, Prof. Don DeVoe, for his support, encouragement, and mentorship throughout my graduate study. It is indescribable how much I appreciated your supervision and enthusiasm in research, as well as your thoughtful guidance for my graduate life.

I want to thank my committee members Profs. John Fisher, Srinivasa Raghavan, Dimitrakopoulos Panagiotis, and Kyu Yong Choi for their guidance and input for my dissertation. I also would like to acknowledge Profs. Amy Karlsson, Benjamin Shapiro, and Dr. Rajesh Krishnamurthy for their kind guidance for developing my early research.

Many thanks go to my friends at Maryland MEMS & Microfluidics Laboratory, Dr. Eric Kendall, Dr. Omid Rahmanian, Dr. Michael Wiederoder, Dr. Alex Sposito, Dr. Prakruthi Hareesh, Supriya Padmanabhan, Dr. Zhu Chen, Dr. Hesam Babahosseini, and our newest members for their constructive discussion and friendship throughout the past five years. Also, I would like to express my gratitude toward my Chemical and Biomolecular Engineering classmates. Many thanks to my Korean friends in the University of Maryland, Korean Graduate Student Association, and Crazy Riders, as well as my wonderful housemates of the Duke street for helping me in so many ways.

My graduate study would have been impossible without my family. I am especially thankful for my parents, Seung Ho Han and Yanghee Kim, for their boundless love, encouragement, and support throughout my life. You have always been my greatest mentors. I also would like to recognize the wonderful support from Sohl and Woosup.

Last, I would like to thank Daeun for her unwavering love. You are my greatest inspiration.

Table of Contents

List of Tables

Table 4.1. Design guideline for Bradley hydrocyclone and dimensions of μHC adjusted for optimal 3D printing quality..... 63

List of Figures

Chapter 1: Introduction

1.1. Lab-on-a-Chip Technology for Point-of-Care Diagnostics

Point-of-care (POC) medical diagnostics offer enormous potential for enabling more rapid, effective, and personalized disease monitoring and treatment.[1–6] Distinguished from the traditional healthcare settings, in which diagnostic testing is performed over large numbers of patient samples using high throughput equipment located in a centralized clinical laboratory, the future of healthcare technology is advancing toward a model where a wide range of diagnostic tests can be performed in near-patient settings, ranging from small clinics to the patient's bedside, to acquire individualized assay results with minimum delay, benefitting the clinical decision-making process and patient outcomes. The application of POC testing has already been successfully commercialized in recent decades, with widely available POC assays including glucose monitoring,[7–10] pregnancy test,[11,12,13] blood coagulation test,[14] and troponin monitoring for acute myocardial infarction (AMI).[15,16] With recent technological advances, POC testing has been further adapted to various genetic diagnostics, enabling early-stage disease detection by analyzing genetic clues in the blood. For example, advanced detection techniques such as electrophoresis,[17] impedimetric sensing,[18–20] colorimetric assays,[21–23] nucleic acid amplification techniques such as polymerase chain reaction (PCR), and advanced optical techniques including surface-enhanced Raman spectroscopy (SERS) have successfully

demonstrated for detection of infectious diseases, inflammatory response, and cancers.[2,24,25]

In 1980s, a new concept called "lab-on-a-chip (LOC)" system was envisioned as a new solution for the development of highly integrated POC diagnostics, and many of the advantages of this approach were outlined in a seminal paper by Andreas Manz in 1989 which introduced the idea of a "micro total analysis system"[26,27] The idea of combining microelectromechanical systems (MEMS) and microfluidic technologies enables miniaturization of conventional clinical lab tests and integration of multiple benchtop techniques into a small device, offering great advantages including short turnaround time, minimal reagent usage, portability, low cost, low energy consumption, and facile mass transport and measurements.[28–30] While numerous studies have advanced the development of new detection techniques capable of enhancing sensitivity and detection limits of diagnostic sensor based on microfluidic technology, other essential components of POC diagnostics such as sample preparation, reagent storage, and fluidic control have received less attention by the research community. The work in this dissertation seeks to address these tasks as essential challenges to realize true POC diagnostics, with a particular focus on improving key aspects of sample preparation, and ease-of-operation for microfluidic POC diagnostics suitable for use in near-patient environments.

1.2. Lab-on-a-Chip Techniques for Clinical Sample Preparation

Molecular targets suitable for POC diagnostics must be analyzed from patient samples that typically consist of complex matrices containing large number of

confounding components including intact cells, proteins, lipids, small molecules, and ionic species that can interfere with effective target identification and qualification. As a result, sample preparation is typically required to isolate and purifying target components from complex biological samples collected from a patient. Conventionally, the quality of sample preparation can be described by the purity of a target component within a processed sample. Insufficient isolation or concentration of the desired target can lead to poor sensitivity or inaccurate results due to the interference caused by other constituents present in the sample. Also, because of the sensitive nature of many biological substances to ambient environmental conditions, maintaining specimen integrity throughout the sampling, storage, and preparation process is a critical concern. Therefore, even in modern healthcare services, conventional sample preparation has been heavily centralized in clinical laboratories where special equipment, reliable sample storage, and highly-trained personnel are available.

A significant advantage of LOC platforms is the potential for sample preparation to be integrated directly into the same microfluidic system used for the assay itself. In established LOC platforms, sample preparation typically demonstrated by isolating target object via microfluidic-based separation techniques by utilizing size,[31–33] binding affinity,[34,35] electrokinetic properties.[36–38] Microfluidic separation can be broadly classified as active and passive techniques by the necessity of external force field to induce the migration of the target. For example, active separation techniques like dielectrophoresis (DEP) and electrophoresis (EP) require electric field, and acoustic resonance focusing (ARF) utilizes piezoelectric elements to generate standing

acoustic waves, and magnetophoresis (MP) needs magnetic bead labeling and electromagnets around microchannel. A strong advantage of active separation is that it can achieve cell separation without pressure-driven fluid flow, eliminating the needs of bulky fluid control accessory such as syringe pump. However, its operation is still limited outside of the clinical facility, because controlling external fields becomes extremely difficult without off-chip controller and the precision of force control also dominantly rely on this equipment.

Passive separation technique only relies on geometry of microchannel and intrinsic hydrodynamic forces.[39,40] A fluid flows within a microchannel generally exhibits the flow profile of laminar flow, which can be characterized by low Reynolds number (Re). At very low Reynolds number, fluid inertia becomes negligible compared with viscous forces and flow behavior can be approximated to the case of Stokes flow. There are many passive separation techniques that take advantage of well-defined streamlines in both low and intermediate Re flow regimes.[38,41–43] For example, deterministic lateral displacement (DLD) is a passive size-based separation technique well suited for effective size-based particle separation during Stokes flow.[44–46] The mechanism of DLD separation is based on the interaction of a particle within the Stokes flow and an ordered array of micrometer-sized posts. Two different particle migration modes can occur within a DLD device; a particle smaller than a critical size flows along the direction of bulk flow, whereas a particle larger than a critical size is forced to migrate into neighboring stream at a gap between microposts, forming isolated streams of particle at different lateral positions. A flow within the intermediate range of Reynolds number, inertial force cannot be ignored anymore. Finite flow inertia brings

various fascinating phenomena, such as inertial focusing, pinched flow fractionation, and Dean flow focusing. Inertial focusing is a phenomenon that particles migrate to equilibrium positions on the cross section of the channel based on the characteristics of particles. This phenomenon is based on the force balance between two inertial forces, the shear-induced lifting force generated by fluid velocity gradient from the center of channel to the channel wall and the wall-induced lifting force caused by the interaction of a particle and the wall.[40,47–49,41,42,50] As mentioned earlier, channel geometry is another essential factor in passive separation techniques. Various studies has revealed that the curved microchannel structure can induce secondary flow that can trigger unique particle movement. A microchannel that has a pinched section shows a unique phenomenon called the pinched flow fractionation. Particles enter into the pinched microchannel forced to align at the same position regardless of the size. When flow meets the broadened microchannel segment, larger particles experience a force toward center of the stream whereas smaller particles experience a force toward the wall yielding separate focused streams of particle by size.[51–53] A related approach employs curved microchannel such as a spiral geometry[38,42] or asymmetric wave shape,[39,50] to separate particles within size-dependent streamlines based on another phenomenon called Dean flow focusing. In a curved microchannel, a secondary flow appears within the channel cross section due to centrifugal forces. This results in two counter-rotating vortices perpendicular to the main flow direction, called Dean vortices. Drag force caused by Dean vortices competes with lift forces between the particles and microchannel walls, enabling particle focusing by size at significantly higher Reynolds numbers than other passive separation techniques.[33,40,45,46,42]

Despite the advancement of microfluidic technologies over the past several decades, realization of LOC separations for effective sample preparation from clinically-important matrices such as blood still poses several challenges, including the need for robust and high-throughput separation, wide range of separability, and simple and easy operation without the need for significant instrumentation or infrastructure. While passive separation techniques such as those described above have partially fulfilled these challenges, typical implementation still requires multiple pumps to manipulate flows precisely, and the techniques are only applicable when the target size is significantly different from other particles in the sample. Thus, developing a new versatile system for clinical sample separation would catalyze the realization of a new generation of LOC platforms for near-patient diagnostics.

1.3. Thermoplastics as Material for Lab-on-a-Chip

Cost is another significant constraint that limits the potential of many existing microfluidic technologies. To become a practical technology, inexpensive and scalable manufacturing is a key challenge for LOC devices. Because LOC technology was originally derived from MEMS fabrication, traditional LOC devices were mostly fabricated in glass or silicon wafers that are high-cost, fragile material for POC testing.[54,55] In addition, bonding of glass or silicon requires high temperature or high voltage process and devices need to be prepared in a cleanroom environment. Soft lithography of silicone elastomers such as poly(dimethylsiloxane) (PDMS) has gained enormous attention from many researchers because of its simple cast-and-cure fabrication, enabling rapid prototyping from a mold prepared via traditional MEMS fabrication techniques. However, the cost of PDMS by weight is higher than silicon,

and the material is not ideal for many POC diagnostic applications due to issues including high water absorption, high gas permeability, and poor solvent resistance. Thus PDMS is unsuitable for practical clinical applications requiring the mass production of low cost POC diagnostics.[55–57] Thermoplastic materials including polycarbonate (PC), polymethylmethacrylate (PMMA), and cyclic olefin polymer (COP) are another common class of materials used for the fabrication of LOC devices. Unlike PDMS, thermoplastics generally exhibits attractive intrinsic properties for LOC application such as inexpensive cost, high optical clarity and low auto-fluorescence over wide range of wavelengths, low water absorption, excellent acid/base resistance, and high bond strength.[58] Among the general class of thermoplastics, COP has been envisioned as a promising material based on excellent UV transparency, extremely low water absorption, and superb solvent resistance.[55,59] In addition, thermoplastic-based LOC devices take advantage of traditional replication-based thermoplastic fabrication methods including hot embossing, injection molding, roll-to-roll printing, micro milling as well as bonding techniques such as thermal fusion bonding, solvent-assisted bonding, and surface modification-aided bonding. Benefitting from these advantages, COP has already begun to be commercialized in various medical products such as pre-fillable syringe, clinical vials, and medicine packaging, making COP a promising material for high performance and low cost LOC devices.

1.4. Dissertation Approach and Organization

This dissertation describes the development of a suite of technologies supporting critical aspects of LOC sample preparation and system automation for POC diagnostics. Because different sample matrices and assay targets present unique

challenges for both sample preparation and automation, this work is primarily focused on the case of diagnostics for the analysis of microbial targets from blood. The aim is to develop novel microfluidic separation systems that are inexpensive, disposable, portable, easily operable with minimal off-chip equipment (e.g. no external electric fields or precision syringe pump), and free of the need for external reagents such as lysis buffer, or affinity-based capture probes.

The dissertation is organized into six chapters. In the following chapter (Chapter 2) an intact separation of bacteria and selective lysis of blood cell from whole blood is demonstrated using a porous silica monolith element integrated into a thermoplastic microfluidic device. Unlike conventional microfluidic size-based separation methods, this study employs a silica monolith with micron-scale pore diameter to induce mechanical lysis of blood cells while allowing intact passage of bacteria with a simple flow-through operation. In addition, selective lysis of blood cells in the device results in smaller cell lysates than chemical buffer-induced lysis, allowing for effective size-based downstream separation by taking advantage of the significant size difference between intact bacteria and other constituents present in the post-monolith flow. The porous silica monolith for whole blood operation is synthesized in a brick format and highly scalable, making large quantity fabrication of the device feasible. Chapter 3 presents a syringe-based microfluidic system capable of reducing the initial blood cell population while also collecting the initial blood specimen from patient. This study employs a novel thermoplastic soft lithography technique to pattern microfluidic features on a thin film that later seamlessly integrated onto a cylindrical body of syringe. Two microfluidic separation techniques are explored in this study,

deterministic lateral displacement and Dean flow focusing. The resulting "smart syringe" integrates a microfluidic separator into a conventional clinical tool, which will aid sample preparation steps without the need for complex instrumentation. In chapter 4, high throughput particle separation is demonstrated using a millimeter scale micro hydrocyclone fabricated via 3D printing. SLA-DLP additive manufacturing was employed to realize a complex internal 3D structure of the micro hydrocyclone (μHC) at the scale of ~100 μm, enabling the realization of microfluidic geometries that are extremely difficult or impossible to achieve using conventional silicon or polymer microfabrication techniques. Together with computer-aided design, an interfacing port that is compatible with conventional tools is readily integrated onto the device, allowing a simple fluidic interfacing. The resulting μHC is capable of separating sub-micrometer particles from milliliters of suspension within a few seconds. This demonstration reveals the promising of high resolution 3D printing for the realization of unconventional microfluidic designs as well as a potential of miniaturized hydrocyclone for clinically-relevant cell separation. In chapter 5, a low-cost, portable, programmable micropump is developed to aid the operation of LOC diagnostics with precise fluid actuation without the need for expensive and bulky precision syringe pumps, making the system well suited for diagnostic applications in resource-poor environments. This technology employs disposable thermoplastic devices integrated with stainless steel screws, and an elastomer ball to not only support integrated pumping but also seal fluids within the device for on-chip reagent storage. Utilizing an Arduino-based microcontroller, precise flow control is demonstrated over a dynamic range of 2 logs, from hundreds of microliters per minute to tens of milliliters per

minute. The resulting micropump operates on a battery pack, and software-defined flow manipulation enables complex fluidic operation such as droplet generation with precision in a completely remote setting. This chapter is adapted from Han et al.[60] Finally, chapter 6 present a summary of the work and primary contributions, and outlines potential future directions for advancing the individual microfluidic technologies and realizing their integration into fully functional POC diagnostics.

Chapter 2: Isolation of Intact Bacteria from Blood by Selective Cell Lysis in a Microfluidic Porous Silica Monolith

2.1. Summary

In this chapter, the isolation of intact bacteria from whole blood is demonstrated through the use of selective lysis of blood cells during flow through an on-chip porous silica monolith. Efficient mechanical hemolysis of blood cells is achieved while providing intact passage of bacteria through the monolith, allowing size-based isolation of bacteria following selective lysis. A process for synthesizing large quantities of both discrete capillary-bound monolith elements and millimeter-scale monolith bricks together with the seamless integration of individual monoliths into thermoplastic microchannels is described. Using this fabrication approach, the impact of monolith morphology, geometry, and flow conditions on cell lysis is explored, and flow regimes are identified wherein robust selective blood cell lysis and intact bacteria passage may be achieved for a variety of both gram-negative and gram-positive bacteria.

2.2 Introduction

The presence of bacteria in the blood stream can lead to serious conditions including sepsis and bacterial infection of other tissues, and rapid identification of blood-borne bacteria is necessary to identify optimal treatment strategies and maximizing the survival rate of patients. The ability to rapidly identify bacteria at or near the point of care would greatly enhance the ability of clinicians to initiate optimal treatment through prescription of appropriate drugs based on the specific infections.

The current gold standard assay for bacterial characterization is based on phenotypic analysis in cell culture, requiring at least 24 h to several days between sample collections, analysis in a clinical microbiology laboratory, and diagnostic answer.[61–63] While phenotypic analysis is relatively inexpensive, this method cannot generate timely results and thus cannot be used to guide the initial stages of treatment.[64]

While analytical methods enabling culture-free detection and identification of bacteria from clinical blood samples are emerging, such as real-time polymerase chain reaction (qPCR),[24] Raman spectroscopy,[25] mass spectroscopy,[65] and infrared spectroscopy,[66–68] these techniques commonly require the isolation and purification of bacteria from blood. The use of affinity capture to immobilize bacteria on magnetic beads for subsequent removal from the initial blood sample has been widely explored.[34,35,69] Magnetic pull-down of bacteria can be highly efficient, but requires the introduction of reagents and instrumentation that complicate assay operation. As an alternative to affinity-based separation, the use of size-based separation of bacteria from other blood components has been demonstrated using various microfluidic platforms employing inertial deflection,[32] inertial lift,[31] or Dean flow fractionation.[33] A central advantage associated with inertial microfluidics for bacteria isolation is that separation may be performed in a continuous flow process without the need for additional reagents or equipment other than a pump to control sample flow in the system. However, inertial separations generally require precise control over flow rates to ensure accurate fractionation and can only be applied to smaller bacteria with hydrodynamic radii that differ significantly from native blood cells. For example,

various strains of *Escherichia coli* and *Bacillus subtilis* have major axis lengths on the order of 6-8 μm,[70] similar to the diameter of human red blood cells.

To overcome the constraints associated with these active separation methods, an alternate strategy involves the selective lysis of blood cells under conditions that do not disrupt target bacteria. In this way a secondary size-based separation may be performed to remove small cell lysate particles, resulting in isolated and purified bacteria for downstream analysis. This approach was recently explored in a microfluidic platform designed for selective chemical lysis a combination of detergent and osmotic shock,[71] enabling highly efficient selective passage of intact and viable bacteria. However, on-chip chemical lysis requires control over multiple solution flows, and the use of detergents or chaotropic agents to permeabilize cell membranes can potentially impact the performance of downstream assays. Additionally, dilution of the lysate is required to prevent damage to target pathogens by ongoing osmotic shock, resulting in low final bacteria concentration using this approach.

In the present work, we explore the use of microfluidic-integrated porous silica monoliths as a simple flow-through method for selective blood cell lysis and intact bacteria isolation. Monoliths are highly porous materials with an open cell morphology that presents tortuous flow paths for fluids forced through the structures.[72] With appropriate control over pore dimensions, the porous morphology serves to induce high mechanical surface stress during cell perfusion through the porous network, enabling mechanical hemolysis of blood cells while maintaining the integrity of bacteria traversing the porous flow path. Using this approach, we show that selective passage

may be achieved for bacteria spiked in human whole blood under flow conditions that yield highly efficient blood cell lysis. The technique is also shown to result in smaller blood cells fragments than chemical lysis, thereby conferring a greater size difference between bacteria and lysate particles for improved downstream separation. Selective passage of intact and viable bacteria was achieved for gram positive as well as gram negative species, in spite of the thinner peptidoglycan layer associated with gram negative bacteria that reduces mechanical robustness of the cell wall.[73,74] The technique is first investigated using small cylindrical monoliths segments synthesized within silica capillaries, and expanded to a higher throughput format using large silica monolith bricks seamlessly integrated into thermoplastic microfluidic chips.

2.3. Materials and Methods

2.3.1. Materials

Tetramethyl orthosilicate (TMOS, ≥99%), ethanol (≥99.5%), methanol (≥99.8%), isopropanol (≥98%), acetic acid (ACS reagent, ≥99.7%), polyethylene glycol (PEG, 10k mw), urea, Tris(hydroxymethyl)aminomethane (TRIS), phosphate buffered saline (PBS, tablet), bovine serum albumin (BSA, powder), and Tween 20 were purchased from Sigma-Aldrich (St. Louis, MO). Methyltrimethoxysilane (MTMS, 97%), sodium hydroxide (10 N, aqueous), and decalin (cis + trans, 98%) were obtained from Alfa Aesar (Haverhill, MA). *Enterobacter cloacae*, *Micrococcus luteus*, *Bacillus subtilis*, and *Lactococcus lactis* were obtained from the United States Department of Agriculture Agricultural Research Service (USDA ARS). Tryptic soy broth (TSB), lysogeny broth (LB), nutrient broth (NB) and yeast extract were

purchased from Carolina Biological (Burlington, NC). Fused silica capillary tubing of 100 μm ID and 360 μm OD was purchased from Molex Connector (Lisle, IL) Upchurch fittings were purchased from IDEX Health & Science LLC. (Oak Harbor, WA). Iridium heat shrink tubing (500 μm initial ID, 250 μm final ID) was obtained from Cobalt Polymers (Cloverdale, CA). Thermoplastic 1020R cyclic olefin polymer (COP) pellets were purchased from Zeon Chemicals (Louisville, KY).

2.3.2. Preparation of Capillary and PMMA Mold

Fused silica capillary was cut into 1 m long segment, then infused with 1 M sodium hydroxide solution. A capillary segment was sealed with the upchurch fittings, then incubated for 3 h in 40 ˚C oven. After incubation, a segment is thoroughly rinsed with deionized water and methanol, and dried in vacuum oven for 6 h at 50 ˚C. A mold for large silica monolith synthesis was prepared by micromachining poly(methyl methacrylate) (PMMA) plates using a computer numerical control (CNC) milling machine (MDX-650A; Roland, Lake Forest, CA). 380 μm and 4 mm diameter endmills were used to make 7 cm long straight channels with 4 mm x 4 mm cross sectional area. PMMA substrates were cleaned by sonication in deionized water and dried completely in vacuum oven. Metastable thermal bonding was achieved by exposing both PMMA substrates under UV/ozone cleaner for 1.5 min and pressed together at 400 psi, 75 ˚C for 15 min.

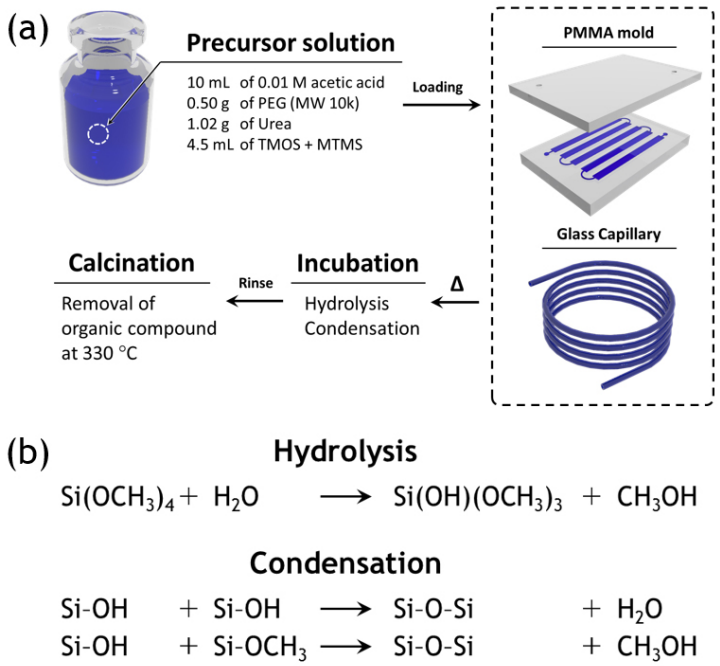

Figure 2.1. (a) Synthesis of porous silica monolith in fused silica capillary and thermoplastic mold via sol-gel chemistry. (b) Competitive reactions during the synthesis of monolith. Silanol groups present on glass capillary form covalent bonding with monolith during this step.

2.3.3. Silica Monolith Preparation

The silica monolith synthesis process, summarized in Figure 2.1, was modified from reported studies.[75–79] The precursor mixture was prepared by adding 0.5 g of PEG and 1.015 g of urea into 10 mL 0.01 M acetic acid solution, and stirred vigorously in an ice bath. Once the components were fully dissolved, TMOS and MTMS 85:15 v/v were mixed and added to the acetic acid solution and stirred for 40 min in an ice bath. The mixed solution was then infused through a 0.22 µm PVDF syringe filter (Millipore, Billerica, MA) into either a silica capillary segment or into a PMMA mold through the same syringe filter. The infused capillary and mold were tightly sealed with upchurch fittings to prevent solvent evaporation, and thermally treated at 40˚C for 12 h, then

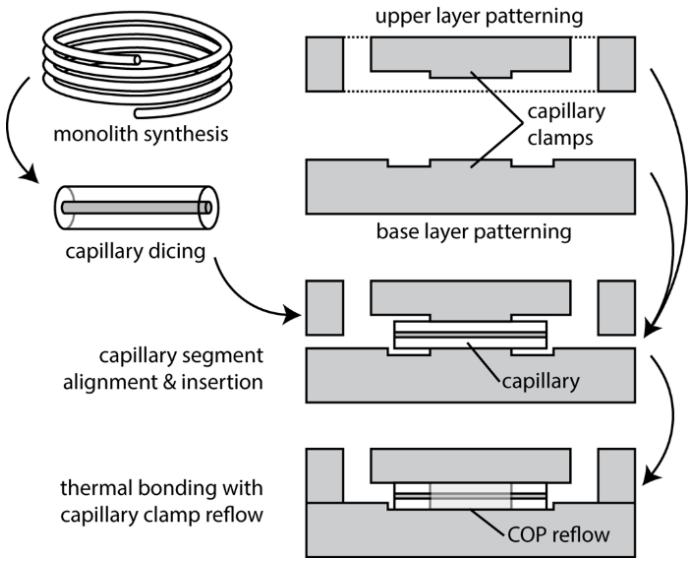

Figure 2.2. Fabrication process for a capillary-integrated monolith chip for selective lysis. Following monolith synthesis and capillary dicing to form short monolith elements, the capillary segments are inserted into a thermoplastic COP chip containing a capillary clamp zone that reflows during solvent bonding to fluidically seal the capillary.

gradually heated to 80 °C over a 6 h period, followed by 15 h incubation at 80 °C to trigger urea decomposition. After thermal treatment, the silica capillary or PMMA mold was allowed to slowly cool to room temperature by natural convection.

To complete the preparation of the capillary monoliths, the capillary mold was cut into approximately 12 cm long segments after discarding about 10 cm from each end and submerged into a large methanol bath for 3 days, followed by submersion in a deionized water bath for 1 day while replacing each solvent every 6 h to remove unreacted reagents. For monoliths synthesized in a PMMA mold, the mold was opened by gently pushing a razor blade into bonding interface, the silica gel rods were collected and rinsed by submersion into a methanol bath for 1 day and deionized water bath for 1 day, with fresh solvents replaced every 6 h. Rinsed capillaries and silica gel rods were dried at 60 °C in an oven for 12 h under atmospheric pressure, then moved into a high

temperature furnace. Calcination was completed by heating at 330 °C for 25 h, removing organic components and leaving porous silica structures. For the capillary segments, an additional 2 cm length from each end was discarded. The remaining middle portion was the cut to desired lengths ranging from 500 µm to 1500 µm using a wafer dicing saw (1006A; Micro Automation) equipped with a diamond blade. Porous silica rods were similarly cut into 2 mm long bricks using the dicing saw.

2.3.4. Microfluidic Device Fabrication and Monolith Integration

Porous silica monolith capillary segments were integrated into COP thermoplastic chips using the process described in Figure 2.2. Upper and lower COP substrates were patterned with a CNC milling machine, using 150 µm and 380 µm diameter end mills to form a short region in the middle and large mating channel features on both substrates, respectively. The channels in each substrate were machined to a depth of 250 µm, except for short regions with a depth of only 75 µm. This shallow region serves as a capillary clamp designed to deform during chip bonding, such that

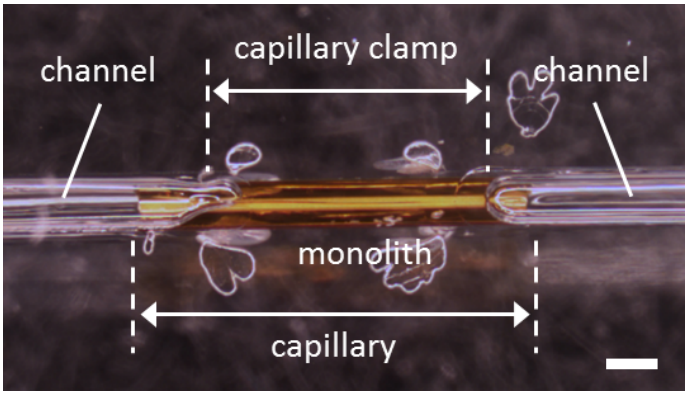

Figure 2.3. Image of a 3 mm long capillary segment integrated within a thermoplastic chip, with reflow of the capillary clamp structures during bonding resulting in complete sealing around the periphery of the capillary. Scale bar is 500 µm.

reflow of polymer in the clamp region fully seals the flow path around a capillary placed in the channel. After machining the chip substrates, each layer was cleaned by sonication in methanol, acetone, and deionized water, then dried overnight in a vacuum oven. Both substrates were next exposed for 1.5 min to a decalin/ethanol (33/67 vol%) solution, which serves to enable solvent bonding of the COP layers as described previously[80,81] and to soften the capillary clamp structures to support polymer reflow during the bonding process (Figure 2.3). After solvent exposure, a capillary segment was manually inserted into the lower substrate channel with the center of the capillary approximately aligned to the capillary clamp structure. The upper substrate was finally placed onto the lower substrate, with the capillary serving to self-align both layers, and the assembly was placed in a hot press to apply a pressure of 500 psi for 5 min at 35 °C.

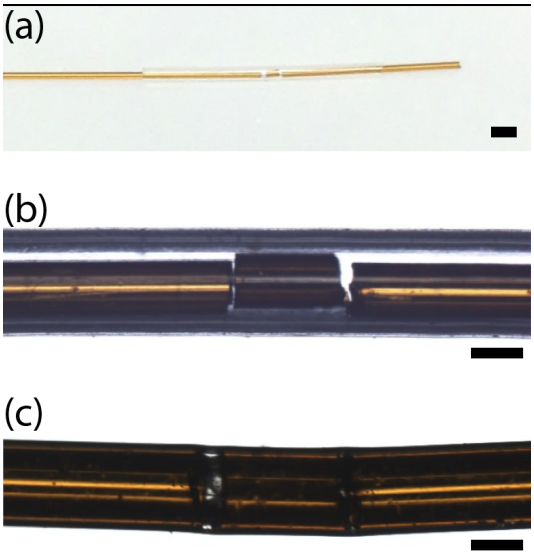

Figure 2.4. Assembly of a capillary monolith device using heat shrink tubing. (a) Porous silica monolith capillary element was placed into a heat shrink tubing segment, with a long inlet capillary abutting the monolith element on end and a short outlet capillary on the other end. (b) Magnified view of the monolith element and inlet/outlet capillaries in the heat shrink tubing before heat activation. (c) The final device heating at 120℃ for 5 min. Scale bars are 500 µm, 1000 µm, and 1000 µm, respectively.

For selected experiments, capillary segments were also assembled with empty capillaries using heat shrink tubing, enabling simpler fluidic interfacing and quicker device fabrication. A porous silica monolith capillary element was placed into a heat shrink tubing segment, with a long inlet capillary abutting the monolith element on end and a short outlet capillary on the other end. The assembly was then placed in an oven at 120 °C for 5 min to activate the heat shrink tubing and permanently seal the flow path (Figure 2.4).

For high throughput device fabrication, porous silica monolith bricks were integrated into COP thermoplastic chips by the process shown in Figure 2.5. Prior to milling, COP pellets were formed into 4 mm and 2 mm thick plaques using a hot press. Using a CNC milling machine, a 2 mm diameter and 3 mm deep hole was first formed

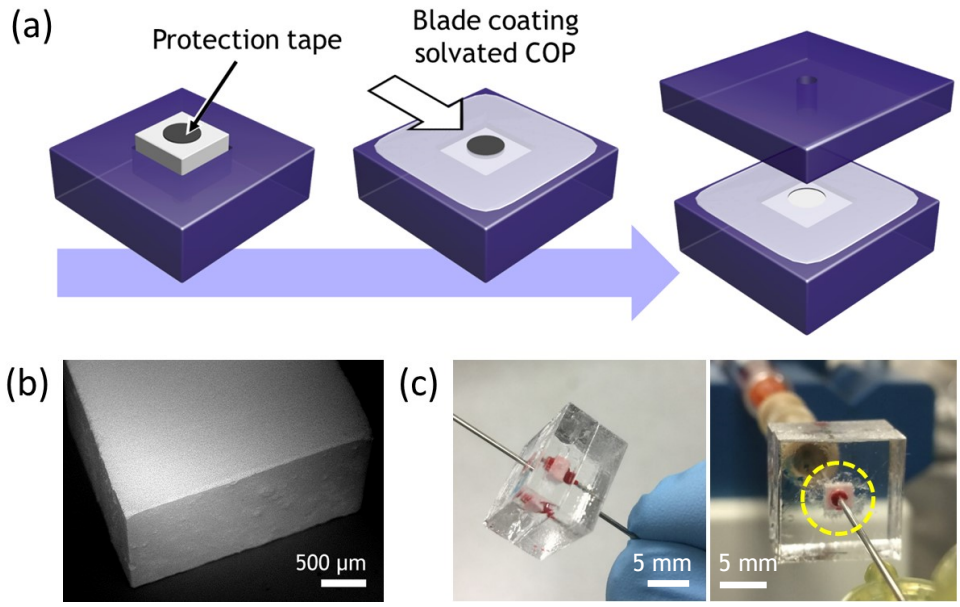

Figure 2.6. (a) Integration process of a large silica monolith brick into a thermoplastic chip. A circular tape is attached to protect fluidic path of monolith brick, and solvated COP is applied via doctor blade. Once it solidifies, protection tape is removed, and device is enclosed with another COP substrate. (b) SEM image of monolith brick cut by wafer dicing saw. (c) A device in operation using whole blood. A red mark appears at the central area of a monolith during whole blood test proves the seamless and stable integration of monolith.

in a 4 mm thick lower substrate, together with a 3 mm square and 2 mm deep socket for the monolith brick, resulting in a square socket for monolith insertion and a 1 mm deep, 2 mm diameter indentation at the bottom of the socket. An additional 3.2 mm wide and 100 μm deep slot was milled around the perimeter of the socket. This slot served as a receptacle for solvated COP to improve sealing of monolith during the final bonding step. Next, a 2 mm diameter and 1 mm deep hole was milled in a 2 mm thick upper COP substrate, and needle ports for external fluidic interfacing were formed on both substrates using a 650 μm drill bit to connect the inlet and outlet needles to the device. Each COP substrate was sonicated in methanol, acetone, and deionized water, and dried overnight in a vacuum oven. A 2 mm diameter circular section of pressure-sensitive wafer dicing tape (blue tape) was patterned using a 2 mm diameter PDMS punch and adhered to the center of a porous silica brick to protect the fluidic path during monolith integration. In this process, the lower COP substrate was exposed to a decalin/ethanol (33/67 vol%) solution for 2 min, and the silica monolith brick was manually inserted into the monolith socket. After insertion, a solvated COP solution, prepared by slowly dissolving COP pellets in decalin to a concentration of 30 wt%, was applied to the lower substrate with inserted silica brick using a doctor blade. The lower substrate was dried for 2 h at room temperature to evaporate decalin and to solidify the solvated COP, after which the protection tape was carefully removed from the monolith. Next, the lower and upper substrates were exposed to the same decalin/ethanol solution for 45 s and 2 min, respectively, and bonded together in a hot press at 300 psi for 5 min at 35 °C. Bonded devices were dried overnight in a 60 °C oven to remove excess solvent.

2.3.5. Selective Blood Cell Lysis and Bacteria Passage

Four bacteria were selected to investigate selective passage through the silica monoliths, namely *E. cloacae* (gram negative, 0.3-0.6 μm diameter and 1-2 μm length), *B. subtilis* (gram positive, 0.25-1.0 μm diameter and 4-10 μm length), *L. lactis* (gram positive, 0.5-1.5 μm diameter coccus or ovoid), and *M. luteus* (gram positive, 0.5-3.5 μm diameter coccus). Each bacteria was obtained as lyophilized powder, and grown in TSB, LB, NB media for 24 h at 25-30 °C with gentle agitation. Resulting bacteria suspensions were pelletized by centrifugation, and re-suspended with autoclaved 1x PBS solution after discarding supernatant. Final bacterial concentration was adjusted to give 30-300 CFU per cultivation plate, enabling accurate quantification of viable bacteria passed through the silica monoliths. For blood lysis tests, whole blood was collected in a 6 mL vacuum container with K2 EDTA sprayed on the interior, and diluted with 1x PBS solution to specified levels prior to use.

2.4. Results and Discussion

2.4.1. Porous Silica Monolith Synthesis

Porous silica synthesis involves a competitive process of sol-gel transition and separation into a co-continuous binary phase via spinodal decomposition of a liquid mixture of alkyl silicates and porogen in acidic solution.[72,79,82] Hydrolysis and condensation of silica are the major reactions which enable the formation of silica glass from liquid alkyl silicate at relatively low temperature.[83] As the chemical reactions progress, entropic loss from the condensation of two silanol groups increases the Gibbs free energy, leading to separation into silicate-rich and solvent-rich phases. Fast

hydrolysis under acidic conditions is required to uniformly hydrolyze most of alkyl silicates, followed by a gradual increase in pH to suppress the hydrolysis and to boost the condensation reaction, which allows homogeneous phase separation in the mixture without macro-phase separation.[72,83,84] As described in Figure 2.1, our silica monolith was prepared from a precursor solution composed of alkyl silicates, PEG as a porogen, urea as a source of hydroxyl ions, and acetic acid as a solvent. The addition of urea in the starting mixture was found to be important for minimizing heterogeneity of porous morphology. Unlike conventional methods for making porous silica, urea can be thermally decomposed at temperatures above 80 °C in the presence of water leaving ammonia and carbon dioxide as products. This allows the hydrolysis and condensation reactions to be separated by increasing the pH of solution during reaction, thereby obviating the need for physical infusion of basic solution which can disrupt the soft gel phase, while enabling a more uniform pH increase throughout the entire gel. A mixture of TMOS and MTMS were chosen as sources of silica to overcome the intrinsic volume contraction associated with a pure TMOS recipe, in which four methoxy groups serve as crosslinking points during the condensation reaction. By using MTMS as an alkyl silicate with only three crosslinking points and one inert group, volume contraction was suppressed so that porous morphology can be uniformly formed without localized shrinkage.

Optimization of this process resulted in monoliths that were homogeneous and well-anchored to the silica capillary walls (Figure 2.6). The excellent attachment of porous silica to the glass capillary is attributed to covalent bonding during condensation reaction between silanol groups on the capillary wall and the growing silica gel phase within the monolith. The thickness of the final skeletal monolith structure was measured as 2.0 ± 0.3 μm, with average through-pore dimensions of 2.4 ± 0.8 μm.

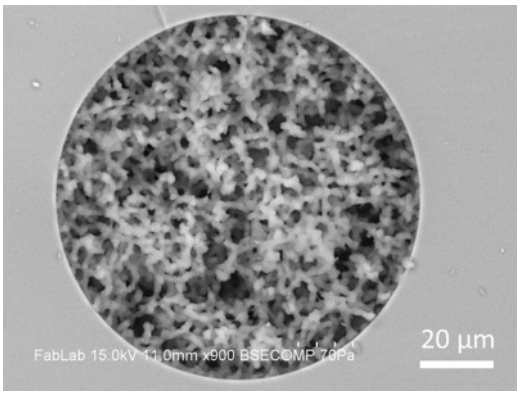

Figure 2.7. SEM image of a silica monolith synthesized within a 100 μm ID fused silica capillary, revealing uniform porosity and excellent wall anchoring of the monolith.

Permeability (K_F) based on superficial velocity was calculated by Darcy's law[78,85];

$$K_F = \frac{\mu u_F L}{\Delta P}$$

Where μ is viscosity of a mobile phase, u_F is superficial velocity, L is length of the silica monolith capillary, and ΔP is pressure drop across the capillary measured by high performance liquid chromatography (HPLC) pump. Permeability (K_F) of porous silica monolith was 2.0×10^{-12} m^2. To minimize the intrinsic variation in sizes caused by hydrothermal treatment and calcination, the resulting capillary was cut into 5 cm long segments and permeability was evaluated before use.

2.4.2. Porous Silica Monolith Integration

The integration of polymer monoliths into microfluidic systems by direct in situ photopolymerization of precursor solutions within on-chip microchannels has been widely demonstrated.[75–77,80,86] To overcome issues of poor patterning resolution, incomplete sidewall anchoring, and large variations in pore size and monolith density associated with in situ polymerization,[87] we previously developed a method for fabricating bare polymer monoliths off-chip, followed by integration of the discrete monolith elements into the final microfluidic system.[88] This process can similarly be applied to silica monolith integration, allowing monolith insertion into chips manufactured from thermoplastics that are incompatible with the high processing temperatures required for in situ inorganic monolith synthesis. While effective, the reintegration process requires the use of trapezoidal channel cross sections and high pressure during bonding to ensure complete sealing of the bare monoliths, often resulting in fracture of the brittle silica structures.

To avoid this complication, two fabrication methods for integrating silica monoliths into microfluidic systems were developed. In the first method, monolith-containing capillary segments was used instead of bare monoliths, allowing the devices to take advantage of the rigid capillary wall which serves as a protective shell surrounding the monolith, allowing high pressures to be used during chip bonding without risk of monolith fracture. This approach eliminates the need for nonstandard channel geometry to ensure proper monolith sealing.[88] A summary of the capillary device fabrication process is presented in Figures 2.2 and 2.3. While capillary clamps are shown on both the upper and lower substrate layers, effective sealing may be

achieved by placing the deforming clamp structures in the upper layer alone, the bottom layer alone, or both layers together.

While the integration of monolith-containing capillaries into microfluidic devices can take advantage of mechanical protection provided by the capillary itself to prevent damage to the monolith during the chip bonding process, the integration and sealing of bare silica monolith bricks presents a different challenge due to the brittle nature of the monolith material. Millimeter-sized monolith rods prepared in a PMMA mold were cut into 2 mm length by dicing saw, yielding small, crack-free monolith bricks (Figure 2.5(b)). To overcome poor sidewall sealing of monolith to COP thermoplastic chip, we utilized the viscous solution of COP dissolved in decalin, leveraging a technique previously reported by our group termed *solvent casting*,[89] in which solvated COP can be applied to various non-flat surfaces and easily solidified by evaporating the solvent. When applied to a COP/monolith device, it can penetrate into the gap between the monolith and COP surface, forming an additional layer of COP surrounding the sides of a monolith. During solvent evaporation, the layer of solvated

COP not only solidifies into a conformal COP film but also forms a permanent bond via solvent-mediated bonding. The application of solvent COP to the porous monolith also results in intrusion of liquid into the surface pores forming an intimate contact with the outer surface of the monolith, thus establishing highly stable sealing between the silica monolith and COP substrate. Unlike other techniques for the ex-situ integration of monolithic elements into microfluidic devices that rely on either precise

contact between the monolith and substrate or the use of highly solvent-softened thermoplastic substrates, the present method was found to provide excellent reliability and leak-free operation even at high pressures required for whole blood perfusion through the devices.

2.4.3. Bacterial Passage and Selective RBC Lysis in a Capillary Device

To explore the efficiency of bacteria passage, we chose *E. cloacae* (gram negative, rod shaped), one of the common cause of hospital-acquired infection,[90,91] and three gram positive bacteria with different shapes and sizes (*L. lactis*, *M. luteus*, *B. subtilis*). Each bacterium was perfused through a series of microfluidic monoliths with varying geometry and under varying flow conditions to evaluate the regimes under which the bacteria pass through the monolith without being lysed.

First, samples of *E. cloacae* suspension and diluted blood were processed through 3 mm long monolith capillary-integrated devices and analyzed by dynamic light scattering (DLS). Despite the shape dependence in light scattering analysis, size difference between erythrocytes and *E. cloacae* were observed in two distinctive ranges for the unprocessed samples, with erythrocytes at 3-6 μm diameter (Figure 2.7(a)) and bacteria at around 0.8-2 μm diameter (Figure 2.7(b)). When analyzing 25× diluted blood, a strong peak at 3-4 μm is observed, reflecting the presence of intact RBCs in the sample. After processing through the monolith, this peak is nearly eliminated, with the primary components at the monolith outlet being particles below 1 μm. In contrast, perfusion of purified *E. cloacae* through the monolith yields no discernable change in the DLS peaks, suggesting intact passage of the bacteria through the system. Chemical

lysis of erythrocytes also resulting in the appearance of smaller peaks, but with a wide distribution ranging from tens of nanometers to several micrometers (Figure 2.7(a)), presumably reflecting the presence of partially exploded cells, small fragments of cell membrane, and cytoplasm released by lysis. These results indicate that monolith passage results in more complete lysis of RBCs than chemical methods.

Similar results were observed from tests using 100× diluted blood spiked with *E. cloacae*, as shown in Figure 2.8. Two significant peaks at around 100 nm and 1 μm match well with corresponding peaks from the diluted blood study (Figure 2.7(a)) and purified *E. cloacae* study (Figure 2.7(b)), respectively. Overall, these initial DLS results indicate that the porous silica monoliths can successfully pass intact bacterial cells while aggressively lysing red blood cells from a mixed clinical matrix.

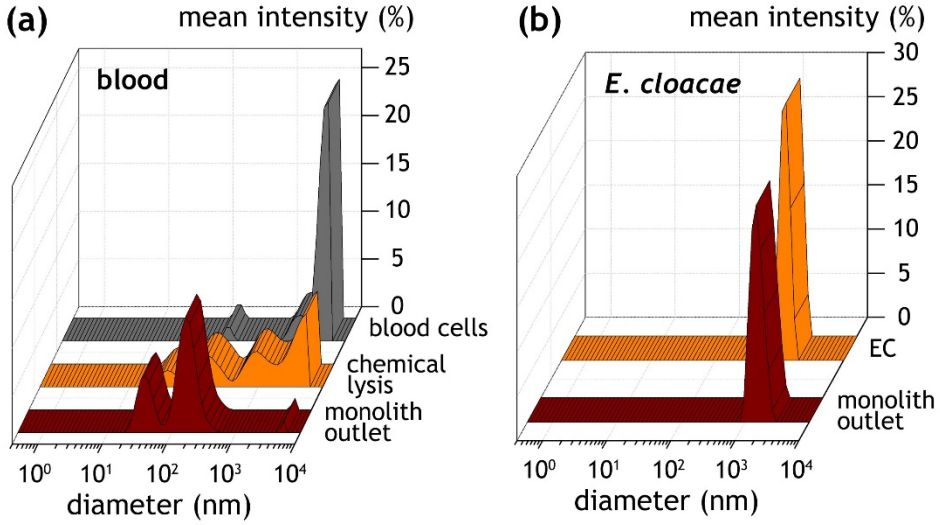

Figure 2.8. DLS measurement of (a) initial 25× diluted blood, chemically lysed blood, and blood lysed by perfusion through the monolith device, revealing a significant reduction in cell debris size for mechanical monolith lysis over chemical lysis. (b) DLS measurement of E. cloacae suspended in 1× PBS, and sample perfused through the monolith device, showing no change in bacteria size.

The RBS lysis efficiency was found to be strongly affected by the length of porous monolith (Figure 2.9). In particular, a wide variation in efficiency was observed for monolith lengths below 500 µm. Despite the efforts to minimize heterogeneity of porous network presented in this study, it has been reported that the porous silica monolith prepared from the mixture of MTMS and TMOS can exhibit up to 30 % variation in the relative standard deviation (RSD) of pore size.[78] While the typical pore dimensions for both the capillary-integrated monoliths and larger monolith bricks were generally consistent with 2.4 µm average pore diameter, the presence of larger through-pores (>10 µm) was also observed, and are believed to be a significant contributor to the high 33% RSD measured for our monoliths.

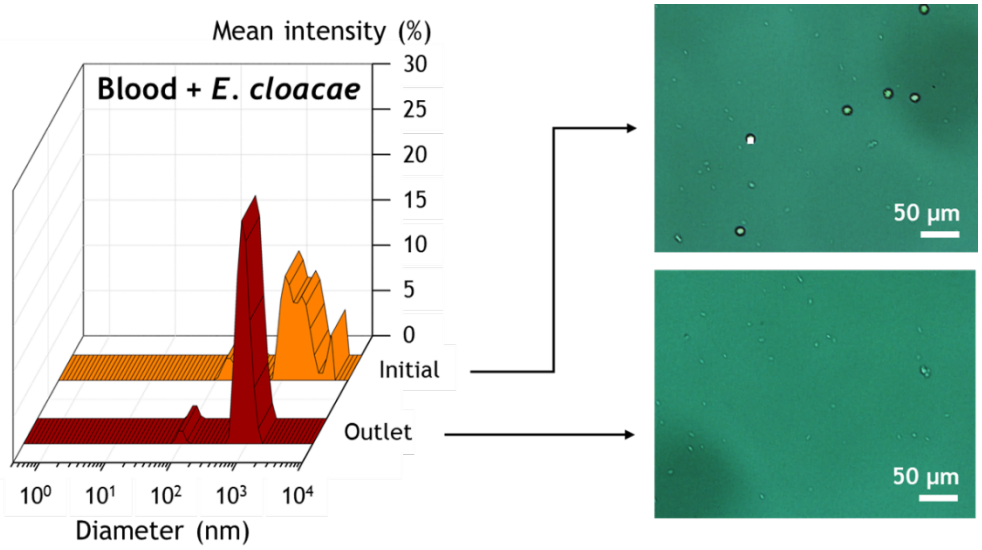

Figure 2.9. DLS measurements of 100× diluted blood spiked with E. cloacae, and sample collected from the outlet of porous monolith. Broadened peak in the inlet sample indicates mixed population of blood cells and small bacterial cells, whereas the outlet sample showed significant reduction in large cell population (> 2 µm), as shown in optical images.

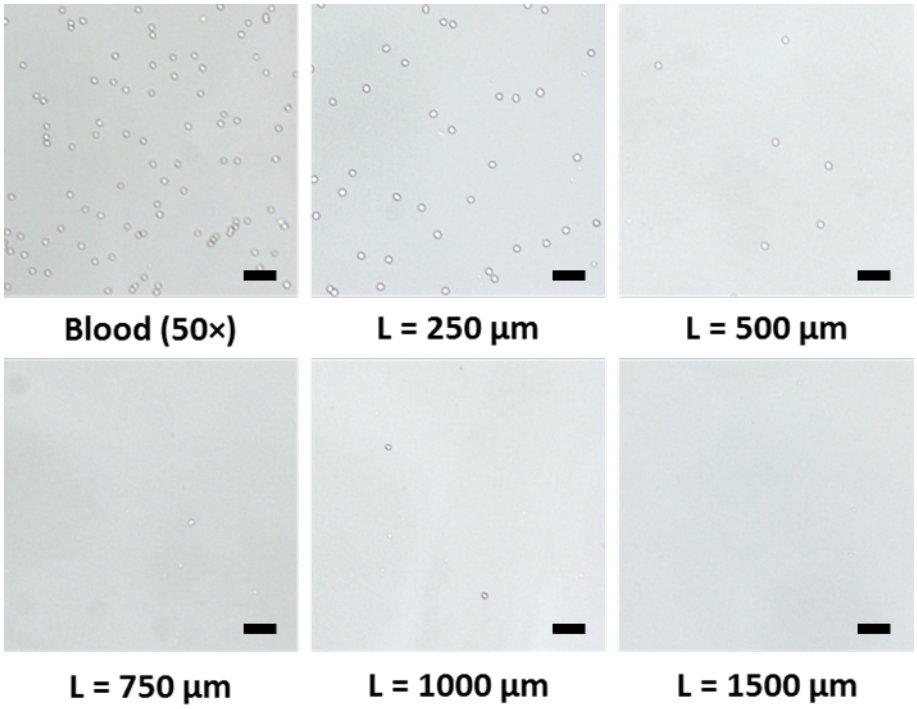

Figure 2.10. Monolith length dependence of RBC hemolysis. 50× diluted blood in 1× PBS was perfused through monolith-containing capillary segments of various lengths at a feed rate of 10 µL/min. Scale bars = 50 µm.

To minimize the impact of variable pore morphology on blood lysis efficiency, we tested different length of silica monolith capillaries at various flow rates. A study of RBC lysis efficiency was conducted using 25× diluted whole blood in TRIS buffer at 10 µL/min. In addition to evaluating erythrocyte lysis, the effects of monolith length and flow rate on the viability of bacteria were also studied using four bacterial strains suspended in TRIS buffer passed through the monoliths using the same experimental conditions as the RBC lysis experiments. To evaluate the passage rate and viability of individual bacterial strains after monolith passage, cells collected from the chip exit were plated and cultured for quantification. The results of these RBC lysis and bacteria viability studies are summarized in Figure 2.10. The RBC lysis efficiency was found

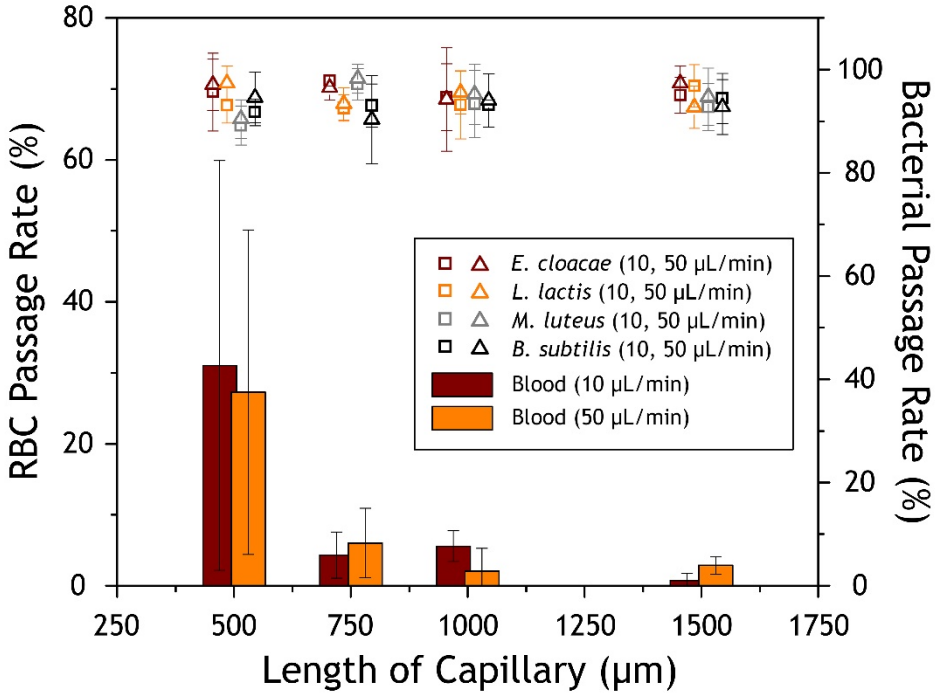

Figure 2.11. Passage rates of RBC and viable bacteria strains at different flow rates and lengths of monolith-containing capillary. Error bars are ± 1 SD.

to significantly increase for monolith lengths above 1 mm, while intact bacteria passage rate remained well above 90% for all monolith lengths tested.

2.4.4. Mechanical Lysis Mechanism

Mechanical hemolysis of human erythrocytes within micro pores under pressure driven flow was initially expected to be a combination of shear stress-driven failure of cell membrane and isotropic membrane tension-induced cell burst. However, the absence of peaks at around the through-pore size in DLS result implies that there were indistinctive "pinching off" of cells, a separation of small spherical globule from the portion of the erythrocytes, which commonly observed in the micropipette aspiration study of blood cells in a high flow shear condition.[92] Also, a dramatic increase in the pressure drop across the monolith segments was observed when less

diluted blood perfused. This supports a scenario of mechanical hemolysis caused by the built-up isotropic tension within the cell membrane by a complete clogging of a pore accompanied with forced deformation of cells beyond its hemolytic threshold.

The human erythrocyte is a discoid shaped cell with sizes of approximately 2-3 μm in thickness and 8 μm in diameter, which presents about 40% larger surface area compared to the surface area of a sphere of the same volume.[93] Combined with its viscoelastic cell membrane, consisting of a glycocalyx layer, a lipid bilayer, and a membrane integral protein network, RBCs can tolerate a high degree deformation at a constant volume and surface area.[94,95] However, when the deformation exceeds a threshold beyond which the membrane surface area must expand to accommodate further deformation, the isotropic membrane tension rapidly increases, and the cells are finally observed to lyse when their fractional area expansion reaches a value of 3%, corresponding to an isotropic membrane tension of approximately 10 mN/m.[96]

When the pore radius is small enough to confine a RBC into a sphero-cylindrical shape with a given cylindrical radius (r_c), the volume (Ω_p) and surface area (Σ_p) are given by[97]:

$$\Omega_p = \pi {r_c}^2 l + \frac{4}{3}\pi {r_c}^3$$

$$\Sigma_p = 2\pi r_c l + 4\pi {r_c}^2$$

$$= 2\frac{\Omega_p}{r_c} + \frac{4\pi {r_c}^2}{3}$$

The corresponding isotropic membrane tension (t_0) of a RBC traveling within a pore in an isotonic condition can be expressed as[97]:

$$\frac{t_0}{K} + 1 = \frac{2\Omega_p}{r\Sigma_p}\left(1 - \frac{2t_0}{\Pi r}\right) + \frac{4\pi r^2}{3\Sigma_p}$$

Where K is elastic area modulus of RBC membrane (500 nN/μm),[98] r is the pore radius, and Π is the osmotic pressure at physiological condition (1.3×10^6 Pa at 25 °C).[92]

Based on these expressions, the isotropic tension in the membrane as a function of pore radius is presented in Figure 2.11. An RBC can flow freely while deforming to fit into a pore when $r > r_c$ (where r_c = 1.53 μm from Figure 2.11), while flow resistance rapidly increases as the pore radius drops below r_c and the system exceeds the deformation limit where membrane expansion can no longer occur without increasing tension. When $r < r_c$, the RBC is forced to stretch further and the membrane tension rapidly increases. Finally, at a critical value of $r = r^*$ (r^*=1.48 μm), isotropic tension of

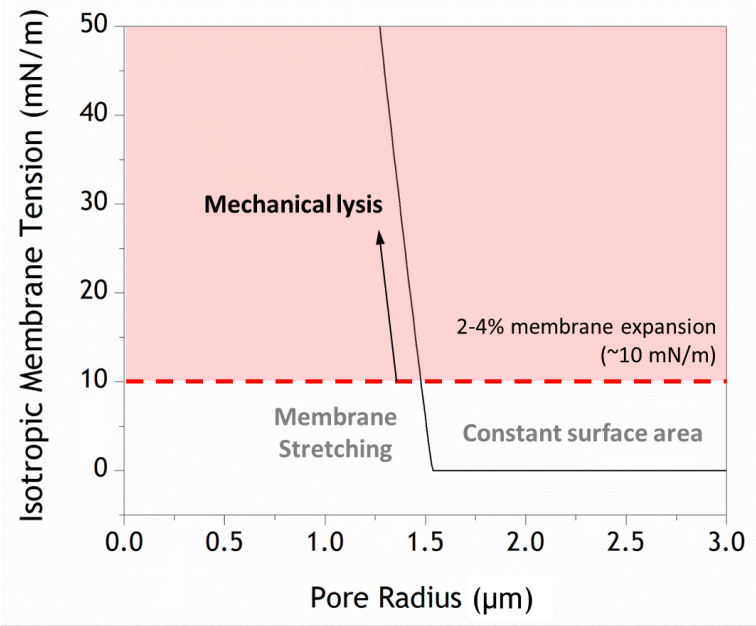

Figure 2.12. Isotropic membrane tension of RBC flows in a pore as a function of pore radius. Fluidic resistance is negligible when pore radius is within a deformable range of RBC, and membrane tension rapidly increases when a pore radius falls below r_c. When the fractional expansion of RBC reaches 2-4%.

the membrane reaches 10 mN/m, and mechanical hemolysis occurs. The porous silica monoliths presented in this study present an average through-pore radius of 1.2 μm, sufficiently smaller than r* to provide high lysis efficiency even in the presence of large variance in the pore size distribution.

2.4.5. High-throughput Bacteria Passage in a Thermoplastic Chip

In the previous capillary device tests, dilution of blood was required because of limited number of pores available for RBC lysis. To extend the capacity of the monoliths to whole blood lysis, centimeter-length prismatic monolith rods with 3 mm square cross sections were prepared in a PMMA mold, resulting in a cross-sectional area increase greater than three orders of magnitude over the capillary devices. Unlike the synthesis of porous silica monolith within a fused-glass capillary, the condensation reaction between the gel phase and the mold is prohibited due to the absence of silanol groups on the PMMA surface. Thus, the periphery of the gel was not constrained, and was subjected to volumetric contraction during synthesis, yielding in significantly smaller pores at the surface of the resulting monolith rods (Figure 2.12). However, because the silica monolith rods were cut to defined lengths using a wafer dicing saw, the bulk internal pore structure was exposed for the final monolith bricks. Based on the results of length dependence study, 2 mm long monolith bricks were employed for high throughput cell lysis and bacteria passage experiments.

The process for integration of a silica monolith brick into a COP device is described in Figure 2.5. Solvated COP applied using a doctor blade enabled seamless

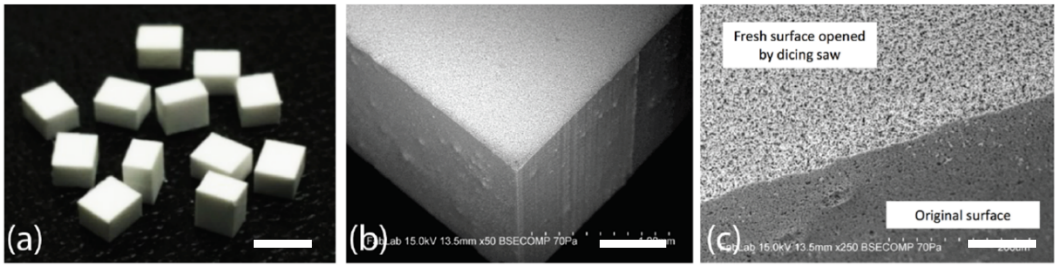

Figure 2.13. (a) Multiple monolith bricks prepared by wafer dicing. (b) Magnified view of a brick corner. The upper surface was formed by dicing, while the two side surfaces were formed by contact with the mold surface. (c) SEM image revealing the desired porosity of the diced monolith surface, in comparison to the closed pores observed on the surfaces in contact with the mold during sol-gel synthesis. Scale bars are 5 mm, 500 μm, and 100 μm, respectively.

filling of any narrow gaps between the monolith brick and mating COP substrate while infiltrating the monolith surface pores to provide excellent mechanical integrity and leak-free flow of whole blood during lysis. During subsequent solvent evaporation, the solvated COP successfully formed a permanent bond to the COP chip surface. Completed devices were capable of processing > 400 μL of whole blood without losing separation efficiency while operating at a flow rate of 10 μL/min.

Whole blood and whole blood spiked with *E. cloacae, L. lactis, and B. subtilis* were employed to evaluate blood cell lysis and viable bacteria passage through the integrated high throughput monolith brick devices. Whole blood was spiked with each bacterial strain originally suspended in 1× PBS, and each sample was infused at 10 μL/min. Individual monolith brick devices were found to be able to process > 400 μL of whole blood before exhibiting a significant increase in back pressure, presumably due to the entrapment of cell debris within the device. Collected filtrate was directly used to analyze RBC lysis efficiency, and diluted 5 times in 1× PBS for bacterial passage rate analysis to obtain 30-300 CFU per plate. In these experiments, an average

RBC lysis efficiency of 99.3 % was achieved, and excellent passage rate averaging 92 % for all four bacterial strains spiked in whole blood was observed (Figure 2.13). A summary comparing viable bacteria passage results for both capillary and high throughput devices is presented in Table 2.1.

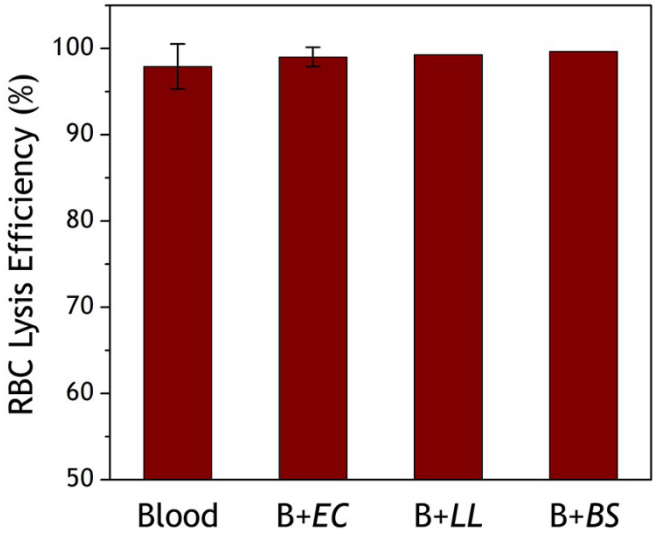

Figure 2.14. RBC lysis efficiency of whole blood in high-throughput devices. Flow rate was fixed at 10 µL/min (EC: E. cloacae, LL: L. lactis, BS: B. subtilis). Error bars ± 1 SD. N=3 for blood and B+EC, and N=2 for B+LL, B+BS.

Table 2.1. Comparison of intact bacteria passage rate of capillary monolith (1.5 mm long) and COP monolith brick (2.0 mm thick) devices.

Species	Capillary device (bacteria only)	High-throughput device (whole blood + bacteria)
E. cloacae	97.4 ± 3.4 %	97.0 ± 5.2 %
L. lactis	92.7 ± 5.3 %	87.4 ± 0.6 %
B. subtilis	92.7 ± 4.1 %	92.5 ± 0.8 %

2.4.6. Serial Operation of High-throughput Monolith Devices

As shown in Figure 2.13, a single high throughput COP device can successfully reduce the population of intact RBCs in whole blood to less than 1 %, however, due to the high density of RBCs in whole blood, this level of lysis efficiency still leaves tens of thousands of intact blood cells per microliter of effluent. While increased lysis efficiency may be possible by extending the length of the monolith, this approach is impractical due to the high fluidic back pressure required to pump whole blood through a long monolith element. As an alternative, passage of sample through multiple high throughput monolith devices was explored. In these experiments, whole blood spiked with bacteria was perfused through a first brick monolith device, and the effluent was collected and introduced through a second monolith brick chip. A Flow rate of 10 μL/min was used for both devices to maintain consistent performance, although in practice the second device is capable of operating at a higher flow rate due to the significant reduction of intact RBC following passage through the first monolith chip.

During initial testing, it was found that approximately 50% of bacteria were lost within the second device during serial operation. This high loss was believed to result from the significant reduction in intact blood cells leading to increased interactions between bacteria and surfaces within the thermoplastic chips, thus resulting in unwanted bacterial adhesion. To maximize bacterial passage during the serial lysis experiments, the use of surface passivation to inhibit bacterial adhesion was explored. We compared surface passivation for PEG, BSA, and a combination of BSA and Tween 20. Although RBC lysis efficiency was maintained above 99% regardless of the surface passivation, bacteria passage rate was greatly impacted by the passivation method.

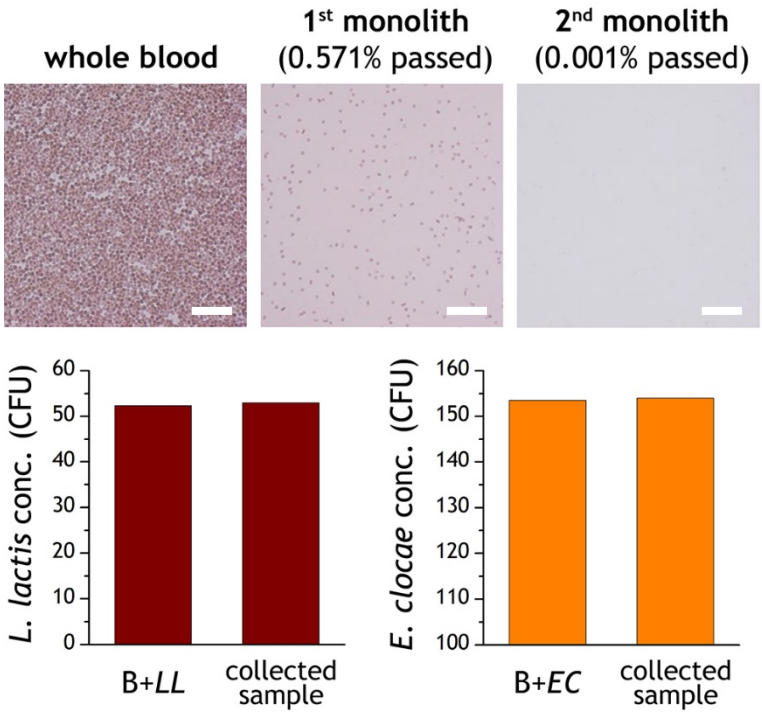

Figure 2.15. Blood lysis and bacterial separation result from serial operation of two monolith. Surface was passivated with BSA/Tween 20. 99.999% of RBC lysis was obtained from whole blood while preserving viability of *L. lactis* and *E. cloacae*. Scale bars = 100 μm.

Optimal bacteria passage was observed for the case of a combined BSA (5 wt%) and Tween 20 (0.05 wt%) solution, which has been reported to optimize surface coverage, with BSA providing bulk passivation while Tween 20 fills the small voids that are sterically limiting for BSA.[18,99] While both PEG and BSA alone did not substantially enhance bacteria passage through the second monolith, the BSA / Tween 20 solution served as an excellent passivation layer. Using this approach, the RBC lysis efficiency was increased to 99.999 % by using two COP devices in series, as shown in Figure 2.14, while preserving nearly the same number of colony forming units of *E. cloacae* and *L. lactis* spiked in the initial whole blood sample.

2.5. Conclusions

Porous silica monoliths enabled highly efficient mechanical lysis of RBCs while passing a range of both gram-positive and gram-negative bacteria without lysis or deterioration of their viability. Selective lysis of RBCs is achieved by forcing the cells to deform beyond their hemolytic threshold, while the presence of a rigid cell wall in bacteria helps to minimize damage to the cells during the passage. The ability to integrate millimeter-scale monoliths using a solvent casting technique allows the fabrication of robust microfluidic devices with seamlessly integrated monoliths presenting large surface areas, greatly expanding the system capacity, with individual monolith devices capable of processing up to 400 μL of whole blood without dilution. Furthermore, serial processing through multiple monoliths enables the complete lysis of all but 0.001% of RBCs in a whole blood sample, together with intact and viable passage of nearly 100% of bacteria. The technology holds promise for rapid preparation of intact bacteria samples from whole blood or other complex matrices containing unwanted cells, with potential for diagnostic applications involving phenotypic characterization of isolated bacteria. Finally, we note that synthesis of monoliths in both capillary and brick formats is highly scalable using batch processing methods, potentially making the resulting devices exceptionally cost effective to fabricate in large quantities.

Chapter 3: Lab-on-a-Syringe: Integrated Blood Cell Reducer Using Conformal Microfluidics

3.1. Summary

A porous silica monolith presented in the previous chapter efficiently induced mechanical lysis of the blood cells, however, the comparative study of capillary device and up-scaled device has revealed that the higher dilution of blood is required for the monolith with smaller cross section. Since the mechanical lysis of a cell requires a cell to be forced to travel through a pore smaller than its size, resulting in a cell occupying a pore until the cell membrane disrupted. Thus, as the number population of cells increases, the required number of pores as well as the chance of severe cell clogging also increase. Therefore, the performance of porous monolith could significantly benefit if a moderate reduction of blood cell can be done prior to the monolith device, allowing larger volume to be processed faster and better. In this chapter, the conformal integration of thermoplastic microfluidic components onto the cylindrical body of a conventional syringe is demonstrated. The hybrid device, designed to combine a small volume blood draw with microfluidic plasma isolation using manual syringe actuation, is presented as once example for the potential of enhancing conventional clinical tools with seamlessly-integrated microfluidic elements capable of adding and simplifying assay steps. Here we employ a commercially available cyclic olefin polymer (COP) syringe combined with a flexible COP microfluidic substrate to perform blood cell reduction directly from a blood draw based on the deterministic lateral displacement

(DLD) and the Dean flow focusing (DFF) techniques, without the need for any external instrumentation or electronic power source.

3.2. Introduction

Thermoplastic microfluidic system benefits from affordable, simple, and rapid manufacturing by utilizing traditional fabrication techniques such as micro machining, injection molding, or hot embossing.[100,101] Unlike the alternative substrates commonly used for LoC device including PDMS and paper, rigid nature of thermoplastic materials and fabrication techniques limited to flat geometry makes its design also bounded in two dimensional. Recently, a new soft lithography technique of thermoplastic called *"solvent casting"* was reported by our group.[89] This technique features a viscous solution of COP prepared by dissolving COP pellets in a decalin, which can be applied similar to PDMS casting process. Once solvent evaporated from the solution, it recovers mechanical rigidity and preserves the negative shape of the mold. Furthermore, remaining solvent within solidified COP can promotes a permanent bonding to another COP substrate. Based on this study, we designed a new smart tool called "lab-on-a-syringe". The lab-on-a-syringe features a microfluidics size-based separation device embedded directly onto a conventional syringe, thus integrating a sample collection and separation process into a single syringe, one of the most commonly used clinical tool.

In this chapter, we report the direct integration of microfluidic elements onto the curved surface of a thermoplastic syringe body, with fluidic interconnects allowing the transfer of collected body fluids from the syringe to the microfluidic device. Two

approaches are explored. First, a DLD element is integrated into a thermoplastic microfluidic substrate to enable blood cell reduction following a blood draw, with actuation for both sample collection and plasma separation performed using the standard syringe plunger. DLD is a powerful passive particle separation technique that sorts particles based on size, with micrometer-level fabrication resolution required to distinguish particles in the size range of blood cells or bacteria.[44,45] Next, spiral microchannel devices employing another passive size separation technique, Dean flow focusing (DFF), were integrated into the COP syringes. A unique aspect of this concept is that the spiral microchannel geometry is realized by wrapping a straight microchannel around the circumference of the syringe body, thus defining the desired geometry to develop Dean vortices and achieve particle focusing. The spiral microchannel geometry was obtained by simply wrapping two layers of thin film COP prepared by solvent casting around the syringe body, with residual solvent drive off following permanent solvent-mediated bonding between the COP films and syringe body. The resulting integrated devices were used to successfully reduce blood cells at the chip outlet. Significantly, efficient separations were achieved using syringe pump control as well as manual thumb actuation of the syringe plunger, suggesting that the resulting technology may be of particular value for application to diagnostics in highly resource constrained settings.

3.3. Materials and Methods

3.3.1. Materials

Thermoplastic Zeonor 1020R cyclic olefin polymer (COP) pellets was obtained from Zeon Chemicals (Louisville, KY), and Sylgard 184 PDMS was purchased from Dow Corning Corporation (Auburn, MI). SU-8 2100 and SU-8 2015 negative photoresists were purchased from MicroChem Corporation (Westborough, MA). Ethanol (>99.5%), phosphate buffered saline (PBS, tablet), and bovine serum albumin (BSA, powder) were purchased from Sigma-Aldrich (St. Louis, MO). Decalin (cis + trans, 98%) was purchased from Alfa Aesar (Haverhill, MA). 4.5 mm thick PMMA sheets were purchased from US Plastics Corporation (Lima, OH). NutriChef vacuum sealer was purchased from PyleUSA Incorporation (Brooklyn, NY). Fluorescent-labeled 1 μm and 8 μm diameter microspheres were purchased from Microsphere-Nanospheres (Cold Spring, NY), and 6 μm diameter fluorescent-labeled particle was purchased from Thermo Fisher Scientific (Waltham, MA). 1 mL COP syringes were purchased from Merit Medical OEM (Salt Lake City, UT). The body of each COP syringe was approximately 8 cm long, with an outer diameter of 1.0 cm.

3.3.2. Thin Film Thermoplastic Patterning by Solvent Casting

Thin COP film with molded microfluidic features were achieved through application of a thermoplastic solvent casting process, which enables the fabrication of pliable solvent-laden thermoplastic substrates containing high resolution microchannel and other microscale structures.[89] First, the desired microfluidic feature was patterned by SU-8 photolithography on a silicon wafer, and its reverse mold was formed by

PDMS soft lithography. After fully curing the PDMS, a solution of solvated COP, prepared by mixing COP pellets with decalin by 27:73 weight ratio, was poured on the PDMS mold and covered with another piece of flat PDMS to obtain a patterned thin film of COP upon curing. Decalin was gradually removed from the COP solution through the bulk PDMS by placing the mold on a custom vacuum curing chuck for 10 h at room temperature. Once cured, the patterned COP film was peeled from the PDMS mold, then subjected to device bonding. A flat film of COP was prepared in a similar procedure, by spin coating solvated COP on a 10 cm silicon wafer at 500 rpm for 55 s, followed by curing on 60 °C hotplate for 4 h while covered with an unpatterned layer of PDMS.

3.3.3. Integration onto a Commercial COP Syringe

The syringe integration of thin film COP patterned with DLD microposts is described in Figure 3.1. First, fresh COP surface was prepared on COP syringe by mechanically polishing outer surface to remove protective coating and labels, and manually drilled to open vias connecting syringe chamber to microfluidic device. Lab-

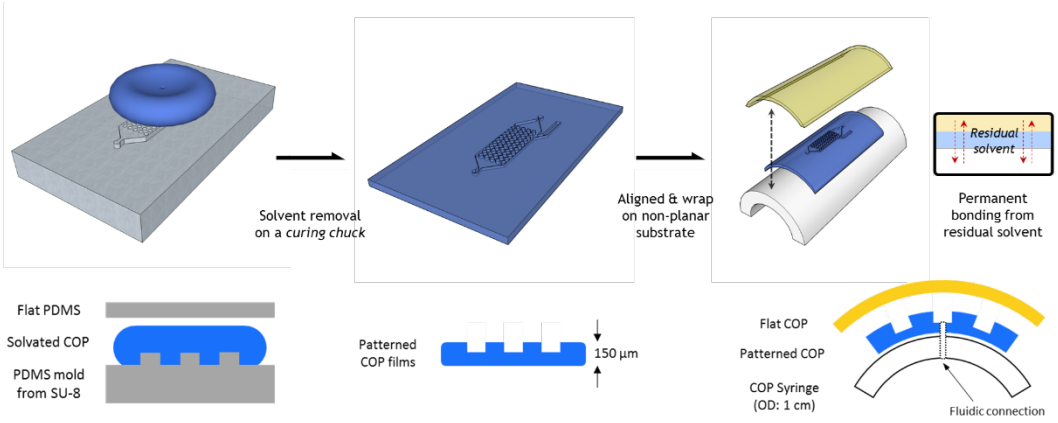

Figure 3.1. Process of fabrication of thin film COP microfluidic device and integration onto non-planar substrate via solvent casting technique.

on-a-syringe device was completed by exposing outer surface of COP syringe to a 35 vol% decalin/ethanol solution, stacked with a patterned COP film and a flat COP film, then sealed in a plastic zip bag using the food vacuum sealer to formulate intimate contact between films and syringe. Bonding was completed by thermally curing it in a 60 °C oven for 10 min. After curing, the device was rested overnight to evaporate excess solvents. Prior to use, microchannels were passivated with 5 mg/mL BSA in 1× PBS solution.

Integration of thin film microfluidic channels for DFF is done in a similar manner. First, two layers of COP film patterned with DFF designs were prepared by solvent casting method as described above. Then, a main channel layer consists of main channel, gutter channel, inlet port, and two outlet ports was aligned perpendicularly to a COP syringe, and stacked with a side channel layer which consists of side channels and alignment marks. Stacked thin films then wrapped around the syringe barrel yielding spiral geometry for DFF separation. Bonding was completed by the same method.

3.4. Results and Discussion

3.4.1. Lab-on-a-Syringe Device Fabricated via Solvent Casting Technique

The lab-on-a-syringe designs explored in this work are composed of a thin film DLD device and a thin film DFF device fabricated by thermoplastic soft lithography technique in a 200 μm thick COP substrate and conformally bonded to the body of a COP syringe. Figure 3.2 describes the precision of solvent casting technique. The DLD design which consists of an array of microposts with 28 μm height and 11 μm gaps,

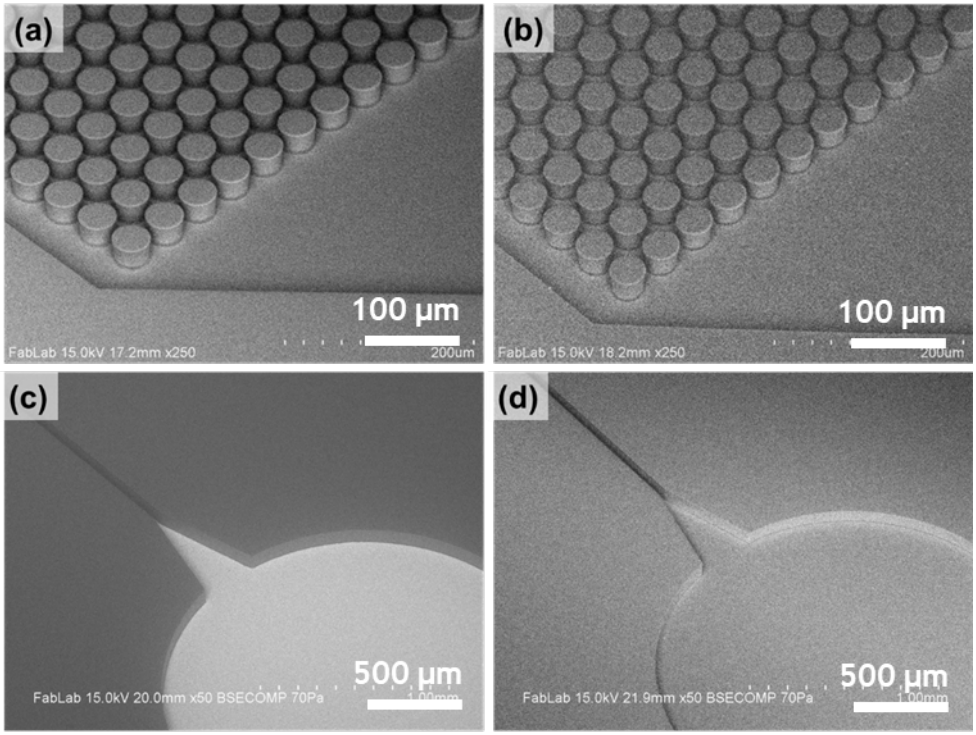

Figure 3.2. SEM images of SU-8 mold and replica fabricated via solvent casting technique. (a) SU-8 mold of a DLD device and (b) COP replica. (c) SU-8 mold of the main channel layer of DFF design near inlet and (d) COP replica.

were successfully patterned into solvated COP from an SU-8 mold and PDMS negative mold, achieving the initially flat substrate to be wrapped around a 1 mL syringe body. The DFF design consists of main channel layer and side channel layer. Main channel layer includes an 8 cm-long straight main channel with a cross section of 100 µm height and 40 µm width and a gutter channel with a cross section of 100 µm height and 300 µm width. Side channel layer consists of 9 side channels aligned perpendicularly to main channel direction and with 2 mm spacing and a cross section of 10 µm height and 50 µm width. Compared to the DLD design which benefits from negligible effect to separation performance caused by the curved surface of syringe, DFF design is only functional when the patterned COP films are wrapped around the cylindrical body of syringe. A straight channel in a main channel layer is naturally forms a spiral when

wrapped on, allowing the Dean vortices to appear within a microchannel which can induce DFF-based separation of particles.

The vacuum chuck used in this study was specially designed to direct solvent removal through the bottom side of a PDMS negative mold by utilizing the gas permeable nature of PDMS. Solvent removal in the vacuum chuck not only minimized unwanted distortion of PDMS from solvent absorption, but also improved casting process by removing air voids through PDMS, obtaining high quality replica with tens of micron feature size (Figure 3.2). Unidirectional removal of solvent also enabled cured COP films to retain the solvent in the side opposite to the vacuumed side, which promotes the bonding to another COP film or a COP syringe surface through the same mechanism of solvent-aided thermoplastic bonding.

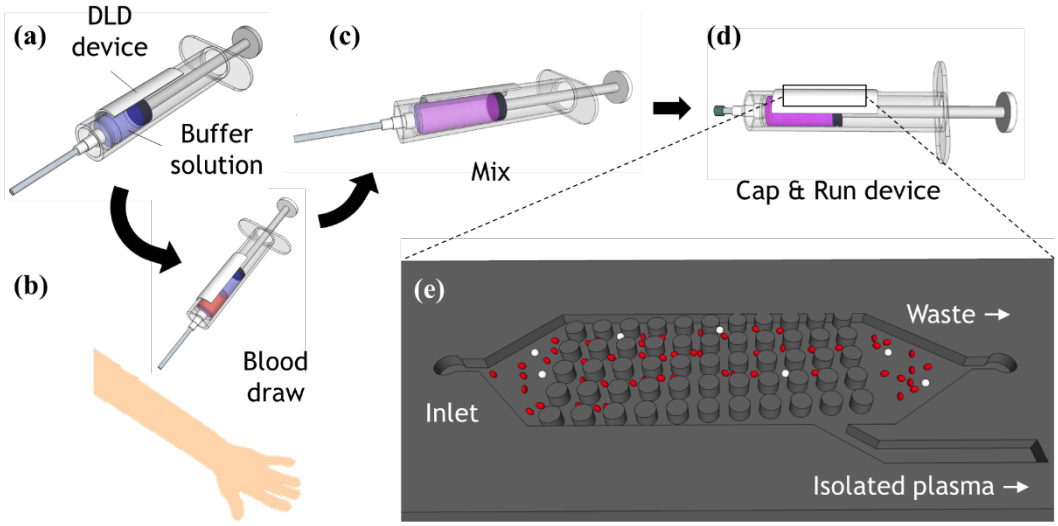

Figure 3.3. Operation scheme of the lab-on-a-syringe device. (a) A device, prefilled with diluent buffer, is used to (b) draw blood from a patient. (c) Manual gentle agitation is done to assure homogeneous mixing, then (d) needle is replaced with a sealed cap to direct flow into the DLD device. (e) Illustration of blood cell reduction within a DLD device.

Integration of microfluidic elements onto a COP syringe was realized by the solvent-mediated bonding by utilizing residual decalin in a cured COP film and the subsequent thermal curing. To formulate an intimate contact between two bonding interfaces, we utilized the food vacuum pump and a sealing bag so that the pressure can be evenly applied on a three-dimensional substrate. Because both the microchannel substrate and syringe were manufactured from COP, no plasticizing or cracking of the syringe was observed.

3.4.2. Size-Based Separation by On-syringe Deterministic Lateral Displacement

Operation of the lab-on-a-syringe device is straightforward as described in Figure 3.3. After drawing blood directly from a patient into the syringe containing buffer, the needle is replaced with a cap and the plunger is depressed to drive sample through the attached microfluidic device. Processed blood with reduced cell population is routed to a collection port, while displaced stream of blood cells returns to the syringe through extra holes to be sequested behind the syringe plunger. Flow rates up to 100 μL/min were achieved by manual thumb press, with no degradation of cell separation performance observed in this range.

Separation performance was first confirmed using synthetic microparticles. The micropost array in a DLD device was designed to have a critical size of separation of 2 μm. Within a micropost array, an incoming flow repeatedly bifurcates at every micropost, forming a complex flow network along the array. For a particle smaller than the critical diameter, a particle is carried into this flow network and its trajectory

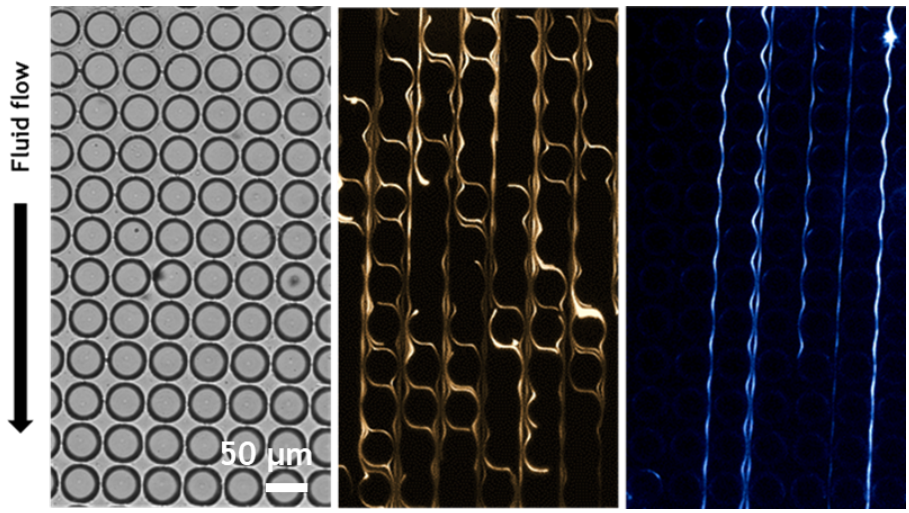

Figure 3.4. Optical image of DLD array. Different particle paths were observed in flat DLD device when fluorescent beads tested; (middle) 1 µm particles proceed in zigzag mode, while (right) 6 µm particles flow in bumping mode.

exhibits "zigzag" pattern along the flow direction (Figure 3.4.). On the other hand, a particle larger than the critical size is constantly deflected by the array of offset posts within DLD device, forcing the larger particle displaced laterally at every micropost. As a result, its trajectory along the micropost array exhibits a straight, bumping pattern. Thus, a flow initially mixed with two particles of different sizes can form two separate particle streams at different position at the channel cross section, allowing size-based particle separation. Separation performance of the DLD design was first examined using 1 µm, 6 µm, and 8 µm diameter microparticles by comparing number population of particles before and after perfused through the DLD device, and the critical diameter was 2 µm. As shown in Figure 3.5, no significant difference in particle population was found for 1 µm microparticles, while up to 92.4% particle reduction was observed for larger particles collected at the particle-free outlet of the device.

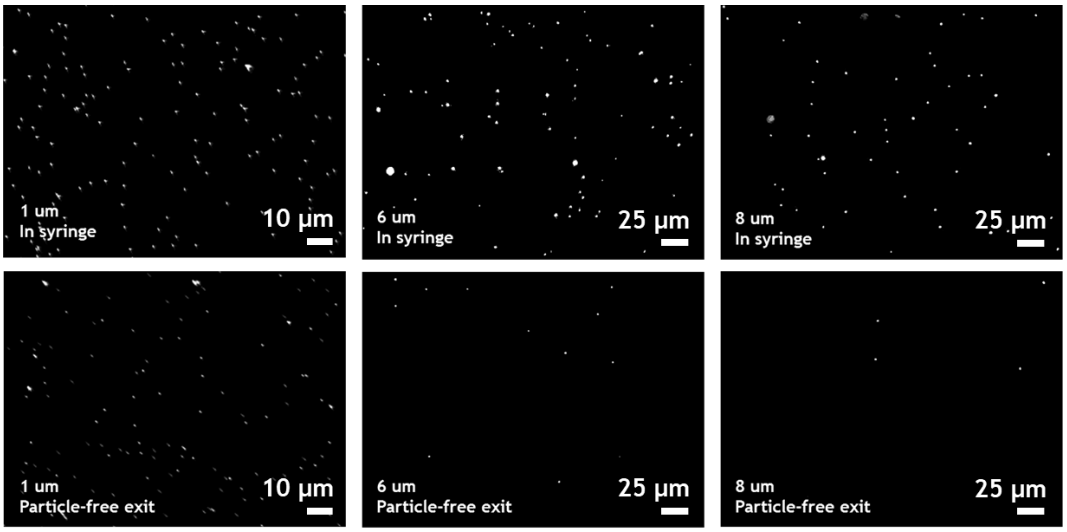

Figure 3.5. Separation of fluorescent polystyrene particles by diameter (upper row) solution before processing through a lab-on-a-syringe device, (bottom row) solution after processed through the device.

When applied to blood, size-based separation was impacted by two major issues. First, increased frequency of cell-to-cell collision induces chaotic deflection, which counteracts the desired lateral migration behavior within the array. Second, the small gaps required for proper separation of blood cells, together with the high number of cells in whole blood results in rapid clogging of the gap near inlet even after treating the surfaces to reduce non-specific binding, thereby decreasing the efficiency of the array dramatically. To achieve useful separations, significant dilution of the initial blood sample was found to be required for the syringe-integrated DLD device. As shown in Figure 3.6, higher dilution level resulted in improved performance, with tup to 80% separation efficiency achieved for 500× diluted blood. While this level of separation offers potential for applications requiring a moderate reduction in blood cell count, the broader utility of this approach is limited by the need for high dilution level, leading to lower analyte concentration and increasing separation time scale due to the larger sample volumes involved.

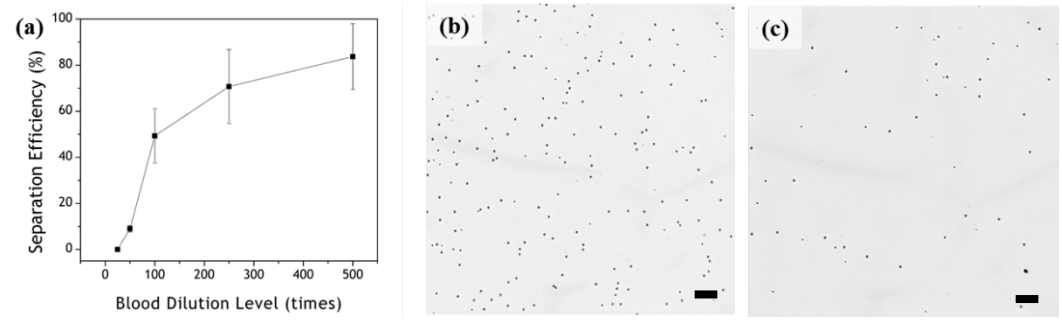

Figure 3.6. Blood cell reduction vs. blood dilution level. Optical images of cell reduction of 500× diluted blood. (b) Before and (c) after processed through the syringe device. Scale bars = 50 μm.

3.4.3. Size-Based Separation by On-syringe Dean Flow Focusing

To limit the need for sample dilution observed for the case of on-syringe DLD separation, we next explored an alternative microfluidic separation method based on Dean flow focusing (DFF), also called spiral microfluidic separation. DFF is a unique particle focusing phenomena observed in a curved microchannel. As fluid flows along the length of a curved microchannel, the parabolic flow velocity profile within the channel is disrupted, leading to the formation of a secondary circulatory flow called Dean vortex. The formation of Dean vortex is caused by the increased contribution of centrifugal force from the curved geometry, and the resulting Dean flow appears perpendicular to the primary flow direction. The intensity of the Dean vortex is characterized by the dimensionless number, Dean number:

$$De = Re\sqrt{\frac{D_h}{2R_c}}$$

$$Re = \frac{\rho U D_h}{\mu}$$

Where D_h is the hydraulic diameter of microchannel, R_c is the radius of curvature of channel path, ρ is the density of fluid, U is the linear velocity of flow, μ is the dynamic viscosity of fluid. At sufficiently high Dean number, two counter-rotating vortices appear exert a net force on particles within the channel. Due to this force, particles can be rapidly focused into size-dependent equilibrium positions within the primary flow. Compared with other hydrodynamic separation methods, this focusing behavior can be achieved very rapidly.

The patterning of a curved flow path with an appropriate radius of curvature is the most essential requirement for DFF separations. Significantly, conventional disposable syringes with outer diameters around 1-2 cm can provide an adequate curvature for micron-scale particle separation using the DFF method, opening the possibility of performing blood separations by taking advantage of the cylindrical geometry of the syringe itself. In this concept, a straight microchannel is wrapped around the outer circumference of the syringe body, allowing particles to be focused at specific radial positions within the channel. Implementation of this concept requires careful design of the microchannel to ensure efficient separation. The channel length required for achieving inertial focusing in a straight microchannel ($L_{f,st}$) and DFF in a curved channel ($L_{f,c}$) are described below:[41,43]

$$L_{f,st} = \frac{\pi \mu h^2}{\rho U_{max} D_p^2 f_L}$$

$$L_{f,c} = f \cdot L_{f,st}$$

Where h is the height of channel, U_{max} is the maximum linear velocity of flow, D_p is the diameter of particle, f_L is the dimensionless lift coefficient, and f is the coefficient for Dean focusing. Empirically found value of the coefficient for Dean focusing varies from 0.2 to 1.0. Thus, for given channel cross section and target size, the rest of DFF channel dimensions can be found from this equation. Channel dimensions of 40 µm width and 100 µm height were selected for main channel and 50 µm width and 10 µm height were selected for side channels assuming a Dean number of 1 at imposed flow rate of 100 µL/min flow, with the channel wrapped around a commercial 1 mL COP syringe with outer diameter of 1.0 cm. Using the unique integration method, a spiral flow path from an 8 cm-long straight microchannel was successfully realized (Figure 3.7)

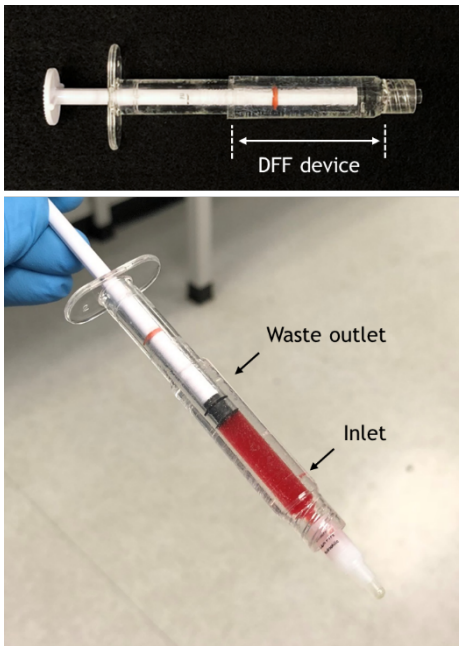

Figure 3.7. Lab-on-a-syringe device with DFF microfluidic separator. Inlet connection is made at the front side of the syringe, and waste outlet was drilled in syringe body to enable the recollection of processed waste into the secondary chamber behind plunger tip. Secondary chamber is sealed with an Viton O-ring (red band in syringe plunger handle) to securely contain the waste.

The lab-on-a-syringe device with integrated DFF channel was characterized to evaluate blood separation efficiency over a range of conditions. The fabricated device was able to process 25 times diluted whole blood with >89% separation efficiency at all tests, showing significantly improved separation at low dilution level compared to the DLD-integrated lab-on-a-syringe device. Blood cell separation tests are summarized in Figure 3.8. Improved separation of DFF method is contributed from Dean vortices, which plays an essential role in the migration of particle and the formation a focused particle stream. As previously discussed, cell-to-cell collision is a

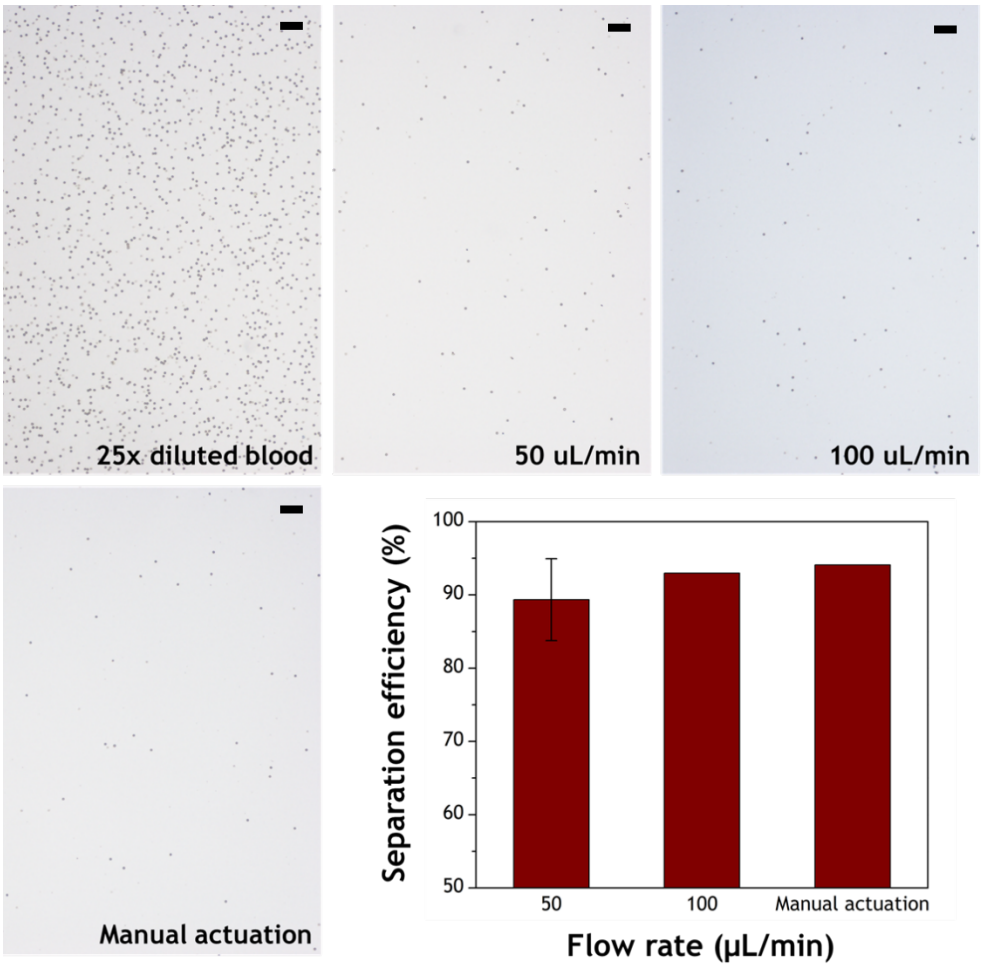

Figure 3.8. DFF-based separation of 25× diluted whole blood operated by syringe pump and manual thumb pressure. N=3 for 50 μL/min flow rate, and N=2 for other results. Scale bars = 50 μm.

typical disturbance observed in low dilution level blood or whole blood. Continuous separation of particles in a microfluidic system typically necessitate a focused stream of particle to enable the collection of particle-deficient portion of the flow by installing a spatially separate outlet at far from the focused particle flow. Increased inter-cell collisions inevitably broaden the particle stream and shrink the particle-deficient zone, making the spatially isolated sample collection more difficult. For the DFF technique, the equilibration points are found at asymmetric position on channel cross section because the Dean vortices constantly recirculating perpendicular to flow direction make possible equilibration points for straight microchannel unstable. Therefore, the focused particle stream in spiral microchannel tends to be located far away from one side of channel, allowing more efficient spatial flow collection as well as higher tolerance to the broadening effect on focused cell stream at lower dilution level. High-throughput operation is another advantage of DFF technique. Reynolds number-dependency of Dean number indicates that at higher flow rate, the intensity of the Dean vortices also increases. Conventional hydrodynamic separation techniques are based upon a premise that the convective force of the flow is negligible to the diffusive force, hence it requires very low Reynolds number. At higher feed rate, the assumption of negligible convective force becomes not valid, and the hydrodynamic behavior deviates from theoretical expectation. DFF method, however, requires relatively higher Reynolds number to induce Dean vortices, and can tolerate much higher Reynolds number up to the scale of one hundred whereas the most of conventional hydrodynamic separation techniques only valid for $Re < 10$. As shown in Figure 3.8, the DFF lab-on-a-syringe showed the maximum separation efficiency of 95.1% and 96.9% at the flow

rate of 50 μL/min and 100 μL/min, respectively. When the lab-on-a-syringe was manually actuated the plunger with thumb press, it showed the maximum separation efficiency of 97.1%, presenting its potential toward the point-of-care operation for the tasks require moderate removal of blood cells, or more importantly, for the needs of preparing the collected sample at resource-poor environments.

3.5. Conclusions

In this study, we presented a new smart tool hybridized with a microfluidic size-based separation device fabricated by a thermoplastic soft lithography technique called "*solvent casting*". Micron-scale features were successfully pattered onto thin films COC, then integrated onto a common thermoplastic syringe, enabling straightforward operation from sample collection and preparation within a syringe. Solvent casting enabled the fabrication of microfluidic devices onto non-flat substrate, opening up a various way to hybridize microfluidic platforms with everyday items. DLD and DFF microfluidic size-based separation methods were presented, and excellent separation efficiency above 89% for 25× diluted blood was observed for all DFF devices, with the aid of syringe pump as well as with a simple thumb press, presenting promising potential of the lab-on-a-syringe for the point-of-care testing.

Chapter 4: 3D-Printed Micro Hydrocyclones for High-Throughput Particle Separation

4.1. Summary

In this chapter, we report the 3D-printed micro hydrocyclone (μHC), enabling high-throughput separation of micron-sized particles from liquid flow at high flow rates the order of tens milliliters per minute. The application of stereolithography-digital light processing (SLA-DLP) 3D printing successfully realized the complex microfluidic design of μHC in hundreds of microns scale. The resulting device can efficiently separate sub-10 μm microparticles from milliliters of solution in a few seconds. Furthermore, SLA-DLP printing offers control over device design with arbitrary 3D dimensions, enabling fundamental investigations of hydrocyclone physics and performance that cannot be easily achieved by traditional fabrication methods.

4.2. Introduction

Solid-liquid separation is the most foreground fundamental for many biological and clinical processes. In the clinical laboratory, isolating a certain type of cell from a clinical specimen or removing cellular components from blood greatly improve the accuracy of diagnostic tests. Bioreactors for large-scale drug production or biomass production necessitate the enrichment step to isolate a target substance from the mixture of feed solution, byproducts, etc.

Conventionally, solid-liquid separation in those area have been achieved via centrifugation or membrane filtration, both benefitting from simple principles of

operation; centrifugal force and size-based retention, respectively.[102,103] However, these approaches present major drawbacks such as lengthy operation, degradation of performance by biofouling, and risks of cellular damage, which limits their utilities especially in clinical applications due to sensitive natures of biological specimen.[104–106] As the lab-on-a-chip (LoC) platform has become more and more important with advances in microfabrication techniques and microfluidics, the separation technologies also have been developing toward the goals of miniaturization, on-site operation, short turnaround time. Microfluidic-based separation techniques are generally categorized into active separation and passive separation. Active separation techniques utilize external forces such as electric field, magnetic field, or acoustic wave, whereas passive separation techniques entirely hydrodynamic forces and microstructure.[40,42]

Compared to various active separation techniques reported in the field, no use of external forces offers a strong advantage to passive microfluidic separation techniques toward more complete LoC system. Filtration and size-based sorting are two major strategies to formulate passive solid-liquid separation. Filtration through an integrated membrane or a microporous structure formed within the device is a straightforward mechanism, however it still suffers from the same inherent problems of macroscale filtration such as bio-fouling and narrow dynamic range of operation. Size-based sorting techniques including inertial focusing, deterministic lateral displacement (DLD), pinched flow fractionation, and Dean flow focusing induce the lateral migration of solid particles within a continuous flow by balancing hydrodynamic forces.[33,39,40,45,46,42] However, high-throughput operation still remains an obstacle

because the hydrodynamic force balance becomes extremely difficult to achieve when flow is not laminar.

Hydrocyclone is a very powerful solid-liquid separation technique utilizing the centrifugal force generated from its unique geometry and flow profile. Taking advantages of simple and extremely high throughput separation, macro-scale hydrocyclone has been an essential separation device in various industrial area including mineral dewatering,[107,108] catalyst recovery,[109] and water treatment.[110] Despite the long history of hydrocyclone, fundamental understanding about the solid-liquid separation within hydrocyclone is still limited to empirical knowledge and numerical simulation of certain designs, mainly due to its complex internal structure and highly turbulent flow appeared during operation. Additionally, the technology has not been broadly adapted to bioseparation area, because relatively small sample volumes associated with clinical specimens or pharmaceutical batch process is far less than the typical feed volume required for conventional hydrocyclone, which is hundreds to thousands of liters. Recently, miniaturized hydrocyclones to centimeter scale have shown the promising potential of micro hydrocyclone (μHC) as a new solution for isolating micron-sized object from a limited volume of feed, making it suitable for various biological processes.[111]

However, μHC still poses two major challenges. First, μHC can exhibit different separation behavior compared to conventional hydrocyclone because of increased Brownian motion which counteracts the directed migration of a particle, or insufficient setting velocity. Second, fabrication of μHC is very challenging because of

the complexity of the design. Geometry of hydrocyclone represented by two famous models, Rietema hydrocyclone and Bradley hydrocyclone, generally consists of a cylinder connected to a conical bottom, a tangentially connected inlet, two axially attached outlets at the top and the bottom of the device, and a smaller cylinder protruding from the top of the device.[112–114] Thus, realizing its three dimensionally interconnected structure in micron scale is almost impossible for conventional microfabrication techniques.

With recent advances in additive manufacturing such as 3D printing, a new pathway was found toward the realization of unconventional microfluidic designs. Stereolithography coupled with digital light processing (SLA-DLP) 3D printing technique utilizes the photosensitive liquid resin and the digital micro mirror device that can generate a series of two-dimensional photomasks by slicing a three-dimensional design. By constructing each layer vertically, SLA-DLP printing can rapidly produce various unconventional microfluidic devices with tens of micron to hundreds of micron-sized features.[115,116]

In this study, we report the first successfully realized single millimeter-sized μHC device with a hundred micron-scale feature sizes, fabricated by SLD-DLP 3D printing technique. Prepared devices successfully separated microbeads from milliliters of suspension within only a few seconds, suggesting a promising potential for the ultrafast separation of clinically relevant samples. Based on theoretical understanding of the forces exerted on a particle within a flow, advanced μHC design was suggested to improve separation efficiency further.

4.3. Materials and Methods

4.3.1. Preparation of Micro Hydrocyclones via SLA-DLP 3D Printing

A Bradley hydrocyclone model was selected as a design guidance to prepare a 1.5 mm diameter μHC for this study[114,117,118], with parameters adjusted for optimal printing quality (Table 4.1).

A 3D stereolithography (STL) file of μHC was prepared in SolidWorks (Dassault Systems Corporation, Waltham, MA). A coned port connector was also integrated for fluidic interfacing, enabling direct connection to a syringe for manual actuation of this device. A μHC STL file was then moved to the printing computer to convert into layered masks, and it was printed at 25 μm z-step resolution using an EnvitionTEC perfactory 4 SLA-DLP tool (Envisiontec Inc., Dearborn, MI). Printed devices were cleaned with isopropanol to remove any uncured resin, followed by the secondary UV curing in an Otoflash post curing light pulsing unit (Envisiontec Inc., Dearborn, MI) to complete photopolymerization process.

4.3.2. Computational Fluid Dynamic Simulation of Micro Hydrocyclone

To validate μHC design and find proper operational condition, the flow path for each μHC designs were simulated using COMSOL Multiphysics software (COMSOL Inc., Burlington, MA) and ANSYS Fluent (ANSYS Inc., Canonsburg, PA). We simplified fluidic ports in design files for the numerical simulation to minimize the calculation loads, while the internal geometry was drawn identically. For COMSOL, the model was imported in Cartesian coordinate system and meshed via COMSOL's automatic mesh operation for fluid dynamic calculation. For ANSYS, the model was

imported in Cartesian coordinate system, and custom meshed with tetrahedral mesh to obtain 450k, 880k, 2 million, and 7 million elements. Fluid was defined as incompressible water for both software. For time-independent turbulence simulation on ANSYS, the realizable κ-ε model and enhanced wall function was used. Calculation was conducted by choosing the semi-implicit pressure linked equation (SIMPLE) as pressure-velocity coupling algorithm with higher-order quadratic upwind interpolation (QUICK) as density interpolation scheme. To account highly rotational flow within μHC, the Pressure staggered option (PRESTO) was chosen as a pressure interpolation scheme. Three feed rates from 5 mL/min to 40 mL/min was calculated until it converged to residual criteria 10^{-5}.

4.3.3. Size-Based Particle Separation Procedure

Solid-liquid separation of μHC was determined by infusing an aqueous solution containing silica microparticles purchased from Microspheres-Nanospheres (Cold Spring, NY). A μHC was connected to 20 mL syringe via F-120 fluidic fitting (IDEX Health & Science, Oak Harbor, WA), and flow rates were controlled by the Harvard PHD 2000 syringe pump (Harvard Apparatus, Holliston, MA). Perfused solutions were collected separately at overflow exit and underflow exit, then analyzed using Nikon LV-100 optical microscope (Nikon Instrument Inc., Melville, NY) and ImageJ software (National Institute of Health, Bethesda, MD).

4.4. Results and Discussion

4.4.1. Basis of Micro Hydrocyclone

Hydrocyclone is a powerful solid-liquid separator widely used in mineral processing and petroleum cracking,[119,120] even in water treatment.[121] Hydrocyclone separation can be achieved via formation of spiral flow path within its body, exerting centrifugal force to a solid particle traveling along this swirling flow. Unlike many hydrodynamic separation techniques, hydrocyclone operates at transient and turbulence flow regime. Although it is difficult to analyze the relationship between design parameters, operational condition, and to estimate the particle separation performance of hydrocyclone due to a complex behavior of turbulence flow, empirically established hydrocyclone models and observations have been a reasonable guidance for designing a new hydrocyclone in various size scale. In this study, we selected Bradley hydrocyclone model, first suggested in 1960s, to build 1.5 mm main diameter hydrocyclone as shown in Table 4.1.[114]

Hydrocyclone can be divided into three major parts; the cylindrical part consisting the upper body of hydrocyclone, conical part consisting the lower body of hydrocyclone, and the vortex finder within a cylindrical part as denoted in Figure 4.1.

Table 4.1. Design guideline for Bradley hydrocyclone and dimensions of μHC adjusted for optimal 3D printing quality

Bradley	**D_i/D_c**	**D_o/D_c**	**L/D_c**	**l/Dc**	**Angle**		
Ratio of dimensions	1/7	1/5	1/3	6.8	9°		
Modified Bradley	**D_c**	**D_i**	**D_o**	**D_u**	**L**	**l**	**Angle**
Size (μm)	1500	300	300	300	1000	8370	9°

When feed flow enters the top of hydrocyclone through a tangentially attached inlet, it flows along the cylindrical wall naturally forming a rotational flow (Figure 4.2). Due to the presence of vortex finder, entering flow cannot directly proceed to the overflow exit, and it keep flows along spiral direction. If inlet flow exceeds a certain velocity, this spiral flow path develops further in the axial direction toward the underflow outlet. If particle density is greater than that of the fluid, particle migrates toward the hydrocyclone wall by centrifugal and buoyant forces. Finally, particles near the hydrocyclone wall exit through the underflow, while the overflow is depleted of particles.

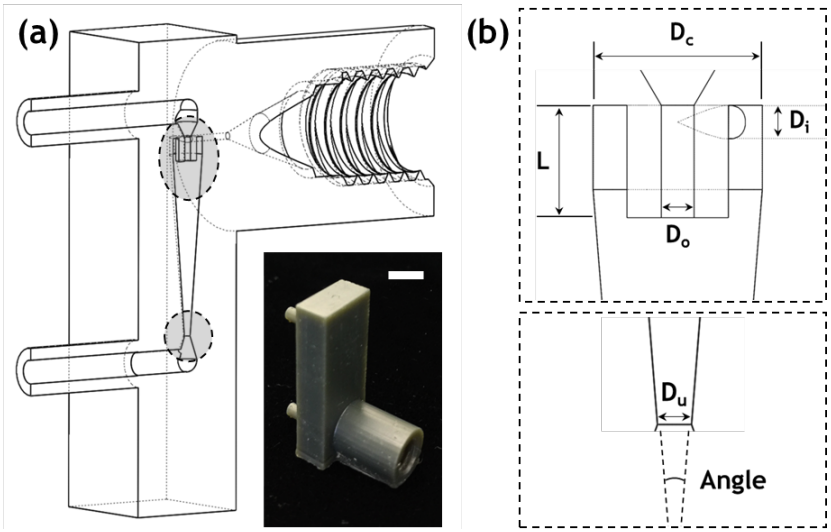

Figure 4.1. (a) cut-through view of μHC and a 3D-printed device. (b) Design parameters for hydrocyclone: primary diameter (D_c), vortex finder length (L), diameters of inlet (D_i), overflow outlet (D_o), and underflow outlet (D_u). Scale bar = 5 mm.

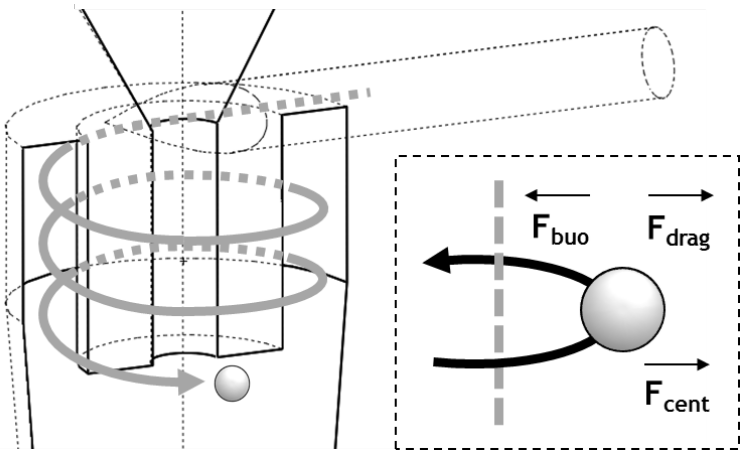

Figure 4.2. Trajectory of a particle within a hydrocyclone and applied forces on a particle in spiral flow path.

4.4.2. Theoretical Analysis of Particle Separation in Hydrocyclone

Although the particle behavior within a hydrocyclone cannot be analytically solved, balancing the major forces exerted onto a particle can provide an insight for optimizing hydrocyclone design and operational conditions. As denoted in Figure 4.2., particle traveling along the spiral path experiences three major forces; centrifugal force, drag force, and buoyancy force. Centrifugal force caused by rotation flow along axial center acting in radially outward direction can be described as below:[122]

$$F_C = m\frac{v_t^2}{r} = \frac{\pi\rho_p D_p^3 \frac{v_t^2}{r}}{6}$$

Where v_t is the tangential velocity of particle, r is the radius of hydrocyclone, ρ_P and D_P are particle density and diameter. Drag force assuming Stoke's flow can be expressed as below:[122]

$$F_D = -3\pi D_p \mu v_r$$

Where μ is the fluid viscosity and v_r is the migration velocity in radial direction. By considering centrifugal force acting as a gravitational force on a particle in radial direction, buoyancy force can be expressed by considering the fluid mass displaced by a particle :[122]

$$F_B = -V_p \rho_f \frac{v_t^2}{r} = -\rho_f \frac{\pi D_p^3}{6} \frac{v_t^2}{r}$$

Where V_p is the volume of particle, and ρ_f is the fluid density.

When hydrocyclone operates at steady-state, the force balance can be achieved between three major forces, then the radial velocity can be expressed as a function of density difference between particle and fluid, size of the particle, diameter of hydrocyclone (D_c), which is twice the radius of hydrocyclone (r), and the tangential velocity:[122]

$$v_r = \frac{v_t^2 (\rho_p - \rho_f) D_p^2}{9 \mu D_c}$$

Based on this equation, tangential velocity, density difference between particle and fluid, particle diameter, and diameter of μHC play an important role in the solid-liquid separation in μHC. In design perspective, both tangential velocity and diameter of μHC are controllable, by either narrowing down the flow path area or scaling down overall system dimensions. Although it has recently reported that the minimum feature size at the order of ten micron can be achieved using the custom resin of polyethyleneglycol diacrylate (PEGDA) in a lab-made SLA-DLP printer,[115] those size range was not achievable in the equipment and the commercial resin used in this study. Instead, the attempt of narrowing down the flow path area aiming to increase the

tangential velocity was demonstrated in the last section. If possible, controlling other key geometries found from analytic model could benefit the separation of biological targets such as red blood cell. First key geometry is the length of vortex finder. Elongated vortex finder will allow an entering particle to stay longer in spiral flow path before it meets the overflow outlet, yielding increased radial migration of a particle. Another key geometry is the main diameter of the hydrocyclone. Although it has never demonstrated, it is generally suggested that smaller main diameter of hydrocyclone will be able to separate smaller size particle better at the same inflow setting.

4.4.3. CFD Simulation of Bradley Micro Hydrocyclone

As described in previous section, CFD calculation was demonstrated to validate the development of spiral flow path within μHC at each operation condition. First, COMSOL simulation was demonstrated to provide initial guidance at low precision simulation setting, then full study was employed by ANSYS Fluent at higher degree interpolation schemes and algorithm for highly rotational turbulence flow within μHC.

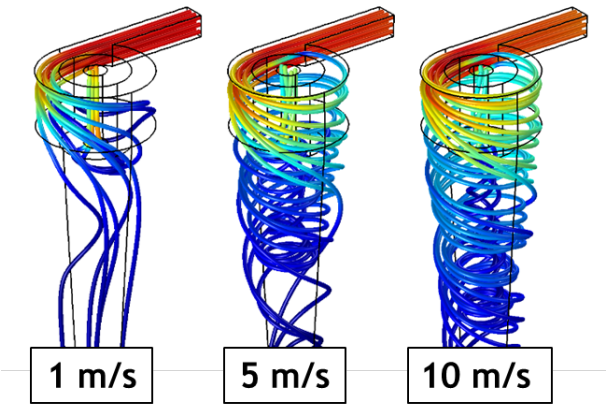

Figure 4.3. Flow path of μHC operating at different inlet velocities simulated by COMSOL multiphysics. 1 m/s, 5 m/s, 10 m/s inlet velocities correspond to 4 mL/min, 21 mL/min, and 42 mL/min volume flow rate, respectively.

As shown in Figure 4.3, insufficient development of spiral flow was found at low inlet velocity, whereas higher than 5 m/s inlet velocity clearly showed the development of swirling flow. Based on COMSOL results, the particle separations were demonstrated at 5 mL/min, 20 mL/min, 30 mL/min, and 40 mL/min.

ANSYS Fluent study showed very similar flow path when calculated at convergence criteria of 10^{-5} for 450k to 7 million mesh elements. As shown in Figure 4.4, µHC operates at 10 m/s inlet velocity exhibits rotational flow throughout the entire body as expected, and also exhibits bidirectional flow along axial center (Figure 4.4(c)) presented as positive vertical velocity at the upper side of µHC and negative vertical velocity at the lower side of µHC. The presence of bidirectional flow together with

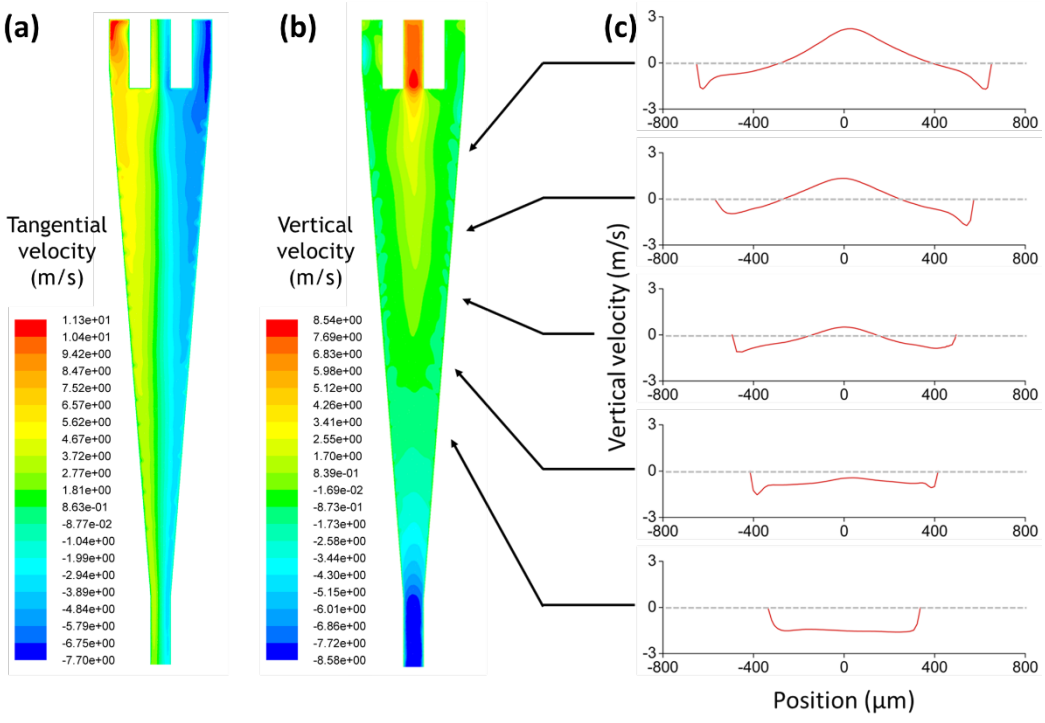

Figure 4.4. (a) Tangential velocity at the center of the modified Bradley µHC operating at 10 m/s inlet velocity. (b) Vertical velocity profile at the same velocity. (c) Vertical velocity plots at different heights of µHC.

highly rotational flow indicates that the flow exiting through overflow exit will be particle deficient due to particle migration outward in radial direction.

4.4.4. High-Throughput Particle Separation in Modified Bradley 1 Micro Hydrocyclone

To compare with simulation results, micro particle separation was demonstrated using 3.7 μm and 7.9 μm diameter silica particles. Particle suspension tests perfused at different inlet velocity were well-agreed with CFD results and expectation based on analytic model, showing lesser particle population at the overflow compared to the underflow at higher flow rates. Similar trends were also found when larger particle is used, showing almost complete separation of 7.9 μm microsphere at 40 mL/min feed rate. Assuming a common blood collection process, a volume of standard blood collection tube (6 mL) can be processed less than 10 s, or less than a minute if a moderate dilution is necessary. To analyze the separation efficiency, we defined the degree of separation by the number population difference between the overflow (N_o) and underflow exits (N_u):

$$\text{Degree of separation } = 1 - \frac{N_o}{N_u}$$

Degree of separation plotted for different particle size and feed rate is summarized in Figure 4.6, showing maximum degree of separation of 0.89 and 0.94 for 3.7 μm and 7.9 μm particles, respectively.

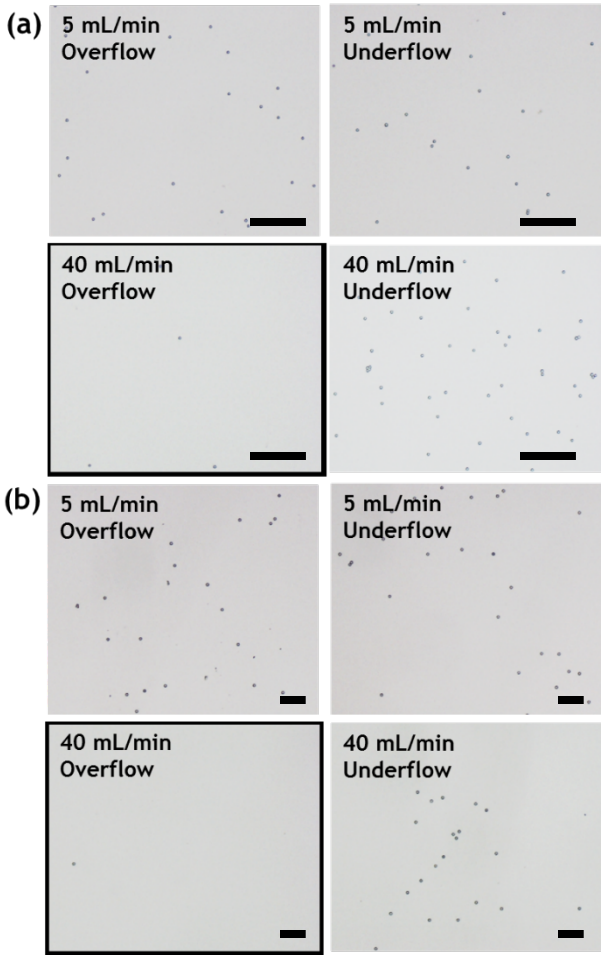

Figure 4.5. Separation of silica microspheres (a) 3.7 µm diameter particles and (b) 7.9 µm diameter particles infused at different flow rates. Samples were collected separately at overflow exit and underflow exit. Scale bars = 50 µm.

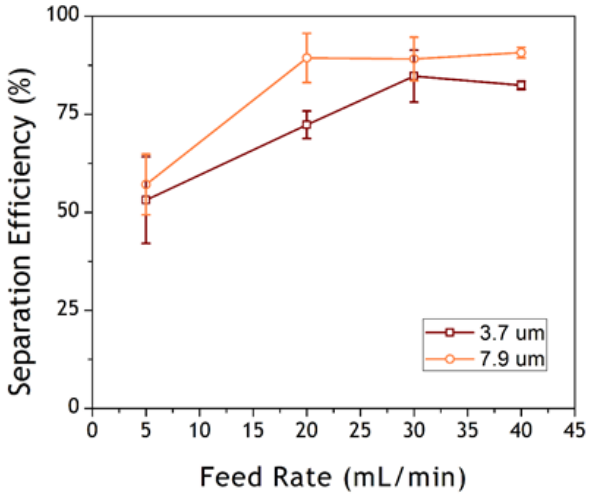

Figure 4.6. Separation efficiency of modified Bradley µHC at different volumetric flow rates.

4.4.5. Enhanced Particle Separation of Modified Bradley 2 Micro Hydrocyclones

As discussed in the previous section, analytic approach to understand particle migration revealed two design strategies to improve particle separation, increasing the tangential velocity and the overall miniaturization of the system. Due to the lower limit in the printable size of the equipment used in this study, design adjustment was only made to narrowed down the gap distance between the vortex finder and cylindrical wall by 50 μm (Bradley 2 μHC), hence increasing tangential velocity within this gap by 44% at the same volumetric flow rate tested for our initial design (Bradley 1 μHC). As expected in the analytic model, increased inlet velocity resulted in increased degree of separation compared to our initial design, as shown in Figures 4.7 and 4.8. Although the actual particle-flow interaction within μHC nor particle behavior in a miniaturized system cannot be simply described by the analytic equation, the result implies that the force balance analysis can provide a useful approach for design improvement and optimization for μHC device.

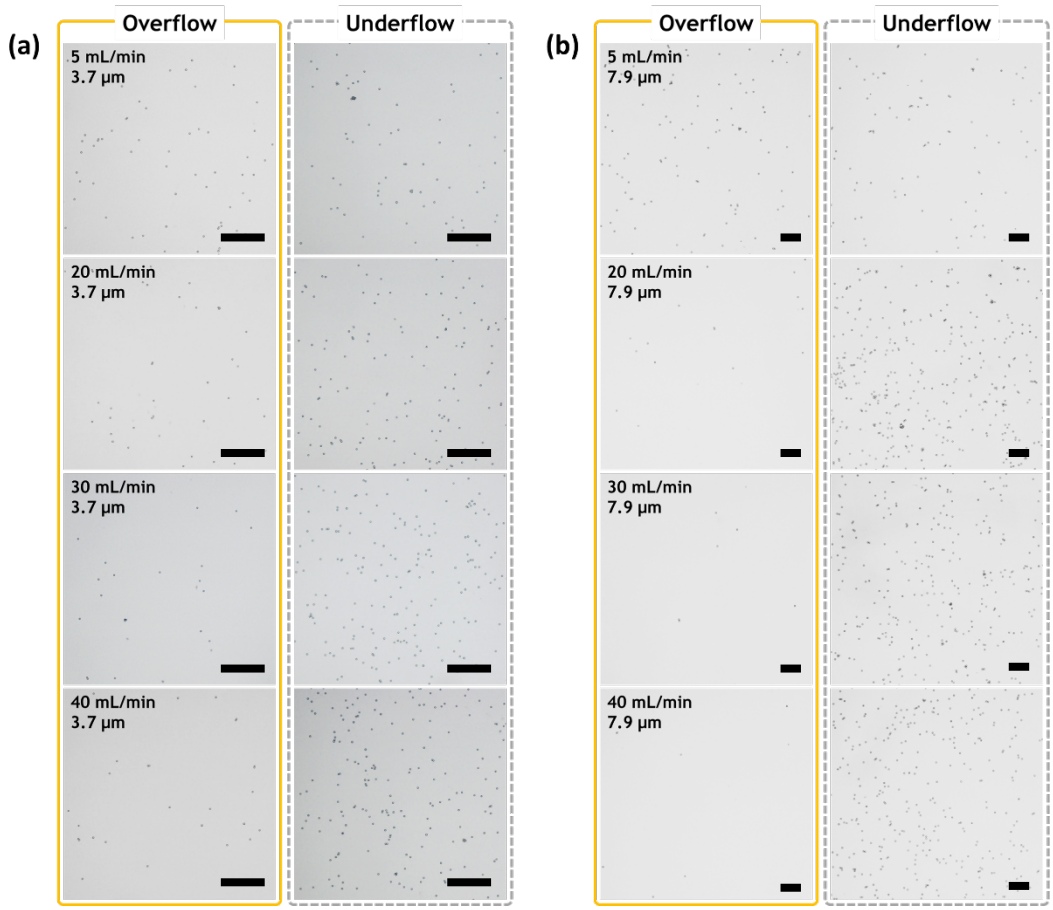

Figure 4.7. (a) Separation of 3.7 µm silica microspheres in the Bradley 2 µHC (b) Separation of 7.9 µm silica microspheres in the Bradley 2 µHC, at different flow rates. Scale bars = 50 µm.

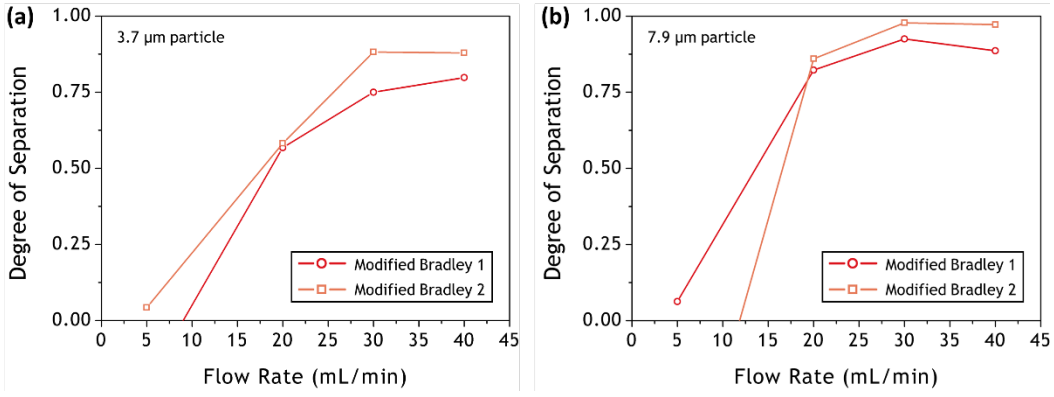

Figure 4.8. Comparison of separation performances between two different µHC models. (a) Data for 3.7 µm particle and (b) for 7.9 µm particles. Modified Bradley 2 µHC showed higher degree of separation at all flow rates above 20 mL/min, with maxima of 0.882 and 0.978 for 3.7 µm diameter and 7.9 µm diameter particles, respectively.

4.5. Conclusions

The application of SLA-DLP printing to complex microfluidic designs such as the μHC platform provides a promising route to the realization of unconventional microfluidic systems. The present work successfully demonstrated rapid and efficient separation of single-micron sized particles, enabling separation of small volume samples suitable for clinical use. Based on theoretical analysis, it successfully shown that performance can be improved even with minor design modification, which presents a promising potential of μHC towards the application in clinical sample preparation.

Chapter 5: Screw-Actuated Displacement Micropumps for Thermoplastic Microfluidics

5.1. Summary

In this chapter, the fabrication of on-chip displacement pumps integrated into thermoplastic chips is explored as a simple and low-cost method for achieving precise and programmable flow control for disposable microfluidic systems. The displacement pumps consist of stainless steel screws inserted into threaded ports machined into a thermoplastic substrate which also serve as on-chip reagent storage reservoirs. Three different methods for pump sealing are investigated to enable high pressure flows without leakage, and software-defined control of multiple pumps is demonstrated in a self-contained platform using a compact and self-contained microcontroller for operation. Using this system, flow rates ranging from 0.5 - 40 μL/min are demonstrated. The pumps are combined with on-chip burst valves to fully seal multiple reagents into fabricated chips while providing on-demand fluid distribution in a downstream microfluidic network, and demonstrated for the generation of size-tunable water-in-oil emulsions.

5.2. Introduction

5.2.1. Fluid Actuation of Microfluidic System

Fluid actuation is an inherent and essential requirement for the operation of all microfluidic systems. For devices designed to operate in conventional laboratory settings, the use of off-chip pumps to control fluid flow enables a high degree of

flexibility in system design, with numerous pump technologies available for achieving a wide range of volumetric flow rates. For example, syringe pumps are nearly ubiquitous in many microfluidics laboratories, with fluid contained in an external syringe body introduced into the microfluidic system based on computer-controlled displacement of the syringe plunger through a motorized lead screw. However, the use of off-chip pumps can be problematic for applications where system cost, size, and complexity are important considerations, such as resource-limited settings, field environments, or small clinics where access to traditional laboratory infrastructure and other resources can be highly constrained. While pump cost can be reduced, for example through the use of additive manufacturing to realize open-source syringe pumps for a fraction of the cost of commercial options,[123–125] the relatively large footprint and added system complexity introduced by off-chip pumps represent distinct disadvantages. Similarly, the need for world-to-chip interfacing between external pumps and on-chip microchannels remains a key challenge for the realization of practical disposable microfluidic assays,[126] particularly when reagents need to be stored off-chip, loaded into pumps, and introduced to a chip through large dead volumes typically associated with interface fluidics.

5.2.2. Micropump Technologies

The direct integration of pumps into microfluidic systems has been the focus of significant research attention over many decades, and offers a path to overcome these limitations. Passive pumping techniques including capillary[127–131] and gravity[132,133] based actuation have been used to induce fluid flow in microfluidic devices without the need for an external power source or manual control, making these methods attractive

for applications demanding automated and zero-power operation. However, passive actuation cannot control flow rates with arbitrary time profiles, and is limited to microfluidic systems with exceptionally low flow resistance. Integrated micropumps employing active actuation can overcome these issues using driving mechanisms such as piezoelectric, thermos-pneumatic, phase change, electrostatic, electrokinetic, electrochemical, or electromagnetic actuation, as summarized in various micropump technology reviews.[134–137] In the case of piezoelectric, electrostatic, and electromagnetic actuation, the use of active pumping can add significant complexity and cost to the microfluidic system due to the need for coupling discrete actuation elements with on-chip microchannels. Electrokinetic actuation can be an effective pumping method, but imposes strict requirements on the working fluid and material system used for microchannel fabrication, and is thus limited in its range of application. Transduction mechanisms including phase change, thermos-pneumatic, and electrochemical actuation have also proven to be attractive for specific applications, although with relatively slow response times as well as low flow rates and pressures that may be generated. Furthermore, in all of the above cases the need for world-to-chip interfacing for reagent delivery remains.

More recently, several integrated pumping mechanisms for microfluidic devices based on manual actuation have been reported. Vacuum driven pumping that takes advantage of the high gas permeability of elastomeric polydimethylsiloxane (PDMS) has been explored for integrated microfluidic systems,[138,139] with either placement of an evacuated PDMS pump element at the microchannel outlet[139] or manual extraction of air from an on-chip reservoir separated from the flow channel by

a PDMS layer[138] used to establish a pressure gradient. Similarly, a variety of elastomer-based pumps designed for simple manual actuation have been reported,[138,140–150] with depression of a PDMS layer used to pressurize fluid in an on-chip reservoir for downstream delivery. An advantage of this latter approach is that reagents may be directly integrated into the microfluidic chip, eliminating the need for challenging world-to-chip interfacing to support reagent delivery. While manual actuation offers a promising approach to microfluidic pumping, particularly for the implementation of assays where simplicity and power minimization are critical concerns, more complex applications requiring accurate flow rates with specific time-dependent flow profiles demand an alternate approach.

5.2.3. Proposed Approaches

Here we describe the fabrication of on-chip displacement pumps capable of precise and time-varying flow control through the integration of screws within threaded reservoirs machined into thermoplastic microfluidic chips. The screw pump concept represents the on-chip analog of a conventional syringe pump, with the machined reservoir acting as the syringe body and the threaded screw serving as both the syringe pump plunger and lead screw. The resulting microfluidic screw pumps are hybrid devices, using low cost thermoplastic substrates and stainless steel screws as disposable on-chip elements coupled with a reusable off-chip control system consisting of a miniature geared DC motor coupled to a microcontroller for software-defined control over pump speed. The fabrication process takes advantage of the excellent machinability of thermoplastic materials, and is fully compatible with existing thermoplastic fabrication methods. By adding fluoropolymer elastomer elements,

comprising either an O-ring attached to a stainless steel rod or a spherical polymer ball, tight seals are realized within the smooth-bored plunger shaft, eliminating fluid leakage within the system and enabling high pressure actuation. Automated pump operation is demonstrated using a microcontroller platform, allowing flow rates to be precisely controlled with linear response over a dynamic range of 2 logs. The pumps are further combined with on-chip burst valves to realize fully-enclosed fluidic reservoirs capable of storing large fluid volumes, enabling true on-demand delivery of reagents without the need for external fluidics or other world-to-chip interfacings. To demonstrate the utility of the resulting pumps for flow control, multiple pumps are integrated into a hydrodynamic focusing droplet generator, with software-defined modulation of the flow rate ratio used to precisely adjust droplet size.

5.3. Materials and Methods

5.3.1. Microfluidic Chip Fabrication

An overview of the thermoplastic chip fabrication process is presented in Figure 5.1. Thermoplastic 1020R COP resin was purchased from Zeon Chemicals (Louisville, KY), and pressed in a hot press (AutoFour/15; Carver, Wabash, IN) to obtain 2 mm thick for microchannel substrates, and 6 mm thick plaques for reservoir substrates. Microchannels for flow rate measurements were directly milled into a COP plaque by a CNC milling machine (MDX-650A; Roland, Lake Forest, CA), with 381 μm and 1 mm diameter endmills, and microchannels for droplet generation were milled with 75 μm and 150 μm diameter endmills. Once channels were patterned, waste reservoirs were drilled through the substrate with a 1 mm diameter bit. Reservoirs were drilled to

a depth of 31 mm into the side of a second 6 mm thick COP substrate using either a 3.5 mm diameter drill bit for seating a Viton O-ring seal, or 2.26 mm diameter drill bit for seating a Viton ball seal. Tapping tools for each screw were purchased from McMaster-Carr (Princeton, NJ). M3×0.5 screw threads were formed by drilling a pilot hole with 2.5 mm drill bit within the first 10 mm of the reservoir, followed by manual tapping with an M3×0.5 tapping tool. Similarly, M4×0.7 screw threads were formed by drilling a pilot hole with a 3.3 mm drill bit and threaded with a M4×0.7 tapping tool. Both COP substrates were cleaned by sequential sonication in methanol, acetone, and deionized water, then dried overnight in a vacuum oven. To smooth residual machining marks in the microchannels, the substrate was exposed to a decalin/ethanol (35/65 w/w) solution for 1 min, followed by rinsing with ethanol and overnight drying. After drying, devices were completed by manually aligning and sealing the microchannel and reservoir layers via solvent bonding by exposing the reservoir layer to a solution of decalin/ethanol (35/65 w/w) and applying a pressure of 2.1 MPa to the two-layer assembly at 40 °C for 5 min in a hot press.

Before sealing each screw reservoir, a defined volume of liquid was added from a pipette to fill the untapped reservoir volume for a total on-chip fluid volume of approximately 50 μL. Sealing of each reservoir was performed using one of three different methods, as shown inset in Figure. 5.1. In the simplest approach, a screw is partially introduced into the reservoir entrance, with sealing provided by deformation of the tapped COP surface during threading of the screw. Stainless steel socket cap screws (sizes M3×0.5 and M4×0.7) were purchased from McMaster-Carr Inc. (Princeton, NJ). The second sealing configuration employed a fluoropolymer elastomer

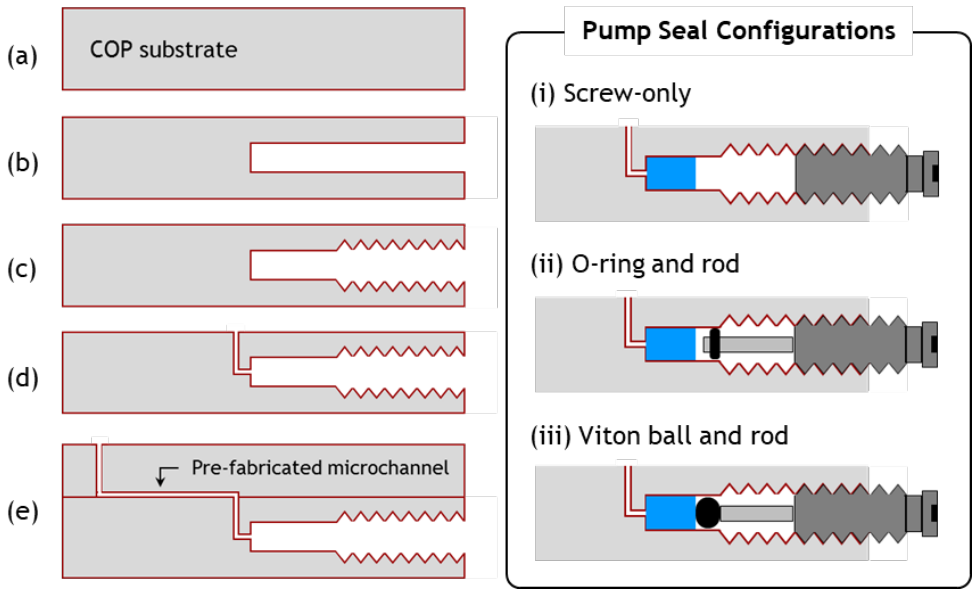

Figure 5.1. Screw pump fabrication process. (a) Starting with a thermoplastic COP substrate, (b) a hole is drilled into the side and (c) tapped to form female screw threads. (d) Vias are milled into the upper surface to connect the drilled hole to a microchannel previously formed in a COP capping layer, followed by (e) solvent-assisted bonding. (f) Pump sealing configurations employed either the screw alone, an O-ring seal, or a ball seal.

(Viton) O-ring assembled onto a 3 mm diameter stainless steel rod (McMaster-Carr). Viton O-rings with 3.6 mm outer diameter and 1.1 mm inner diameter were purchased from Precision Associates (Minneapolis, MN). The rod was first cut into cut to 1.2 cm long segments. A groove, 0.9 mm deep and wide, was formed around the full circumference near one end of the rod using a lathe, and an O-ring was seated into the groove. The chip reservoirs were treated with a solution of cyclohexane/ethanol (1/10 v/v) for 2 min to temporarily soften the inner walls of reservoir and form a smooth surface to enhance O-ring sealing. The assembled sealing rod was manually inserted into the on-chip reservoir, and a screw was threaded into the port until it touched the exposed end of the rod. In the third sealing method, the O-rings were replaced with 2.38 mm diameter Viton balls (Precision Plastic Ball Company, Franklin Park, IL) with

diameters of either inserted into the reservoir bores, followed by introduction of a stainless steel rod and screw.

5.3.2. Pump Control

To enable automated software-defined pump control, a small form factor microcontroller board (Pro Trinket, Adafruit, New York, NY) based on the Arduino physical computing platform was employed. The microcontroller was interfaced with a compact DC motor coupled with a 1000 : 1 gearbox, providing a stall torque of 9 kg cm and no-load speed of 32 rev/min at 6 V coil voltage (Micro Metal Gearmotor, Pololu Corporation, Las Vegas, NV). A shaft coupler consisting of a stainless steel rod (0.635 cm diameter, 2.54 cm length) and shaft adapter (1/4 inch to 3 mm adapter; Servocity, Winfield, KS) was fixed to a hex driver for convenient connection between the output shaft of the gearbox and the pumping screw integrated into the microfluidic chip. Software control of the screw bit rotation speed was achieved by modulating the average voltage applied to the DC motor through an 8-bit pulse width modulation (PWM) signal generated by the microcontroller with a base frequency of approximately 500 Hz. A 5 V voltage source consisting of a 6 V battery and 5 V voltage regulator was connected to the motor through a power MOSFET (IRF520, Vishay Intertechnology, Malvern, PA) for switching the applied motor voltage directly from the microcontroller's PWM output.

5.3.3. Pump Performance Characterization

Linear fluid velocity resulting from pump actuation was determined by sealing a volume of water containing food coloring within the on-chip pump reservoir. The resulting fluid motion within a downstream serpentine microchannel connected to the reservoir was monitored using a digital camera at 60 frames per s. Average flow velocities were determined based on the time required for the fluid front to traverse a known channel length. Volumetric flow rates were then calculated based on the known microchannel dimensions. Flow rates were controlled by varying the duty cycle of the PWM signal applied to the geared DC motor with 8-bit resolution. Theoretical flow rates were determined based on the applied motor speed, screw diameter or reservoir diameter, and thread pitch.

Analysis of leakage pressure past the reservoir seals was performed using a liquid chromatography pump (PU-2089; Jasco, Easton, MD) connected to each COP device through a stainless steel needle press-fit into the outlet reservoir.[151] The COP device under test was filled with DI water prior to the measurement. Under constant infusion of water at 1 μL/min from the outlet, pressure within COP device was monitored with 0.1 MPa resolution. Sealing pressure of each device was determined when a sudden drop in measured pressure occurred, with leakage verified by optical observation of the pump seal region.

5.4. Results and Discussion

5.4.1. Device Fabrication

Thermoplastics are attractive materials for disposable microfluidic assays due in part to their exceptionally low cost, which is nearly two orders of magnitude lower than that of PDMS by weight. Unlike PDMS, an elastomeric material that has been widely used to achieve on-chip pumping in a variety of ways,[137–139,141,147,152,153] the ability to integrate similar micropumps into thermoplastic devices is limited by the high stiffness associated with typical engineering thermoplastics. However, in contrast to elastomers, a key advantage of thermoplastics lies in the excellent machinability of these materials, allowing conventional machining operations such as milling, drilling, and tapping to be harnessed for device fabrication. Here we take advantage of these conventional machining methods to realize miniaturized screw-actuated displacement pumps integrated directly into COP thermoplastic chips. The process flow, depicted previously in Figure 5.1, begins with drilling reagent reservoirs into the side of a 6 mm thick COP plate with endmill diameter dictated by the dimensions of the screw used for pumping. The use of a relatively thick reservoir substrate was necessary to provide sufficient material to support formation of the reagent reservoirs and screw ports. While the manual actuation of screws inserted into the upper surfaces of thermoplastic microfluidic devices has been previously reported by our own group[151,154] and others,[21] the current approach of positioning the screws in the side of the chip substrate enables the formation of significantly larger reservoir volumes for on-chip reagent storage, as well as providing sufficient port depth to support the integration of secondary sealing elements between the screws and stored fluids. Tapping of the reservoirs to form

threads for the pump screws was straightforward, although aggressive sonication was found to be necessary to fully remove tapping debris from the ports.

5.4.2. Software-Defined Flow Control

An image of a custom controller containing two independent pump motors is shown in Figure 5.2(a), and sequential images showing controlled fluid flow through a coupled microchannel are shown in Figure 5.2(b). The stand-alone system consists of two geared DC motors with a coupler and hex key driver attached to each output shaft, a microcontroller, motor drive transistors, and regulated 5 V voltage source. By stacking the circuit layer, motors, and batteries, the resulting controller is compact, with a footprint less than 6 cm square.

Using this controller, volumetric flow rates were measured for pumps using both M3 and M4 screws with Viton ball seals, with results shown in Figure 5.3. Based on the screw thread pitch and fabricated reservoir diameter, theoretical volumetric

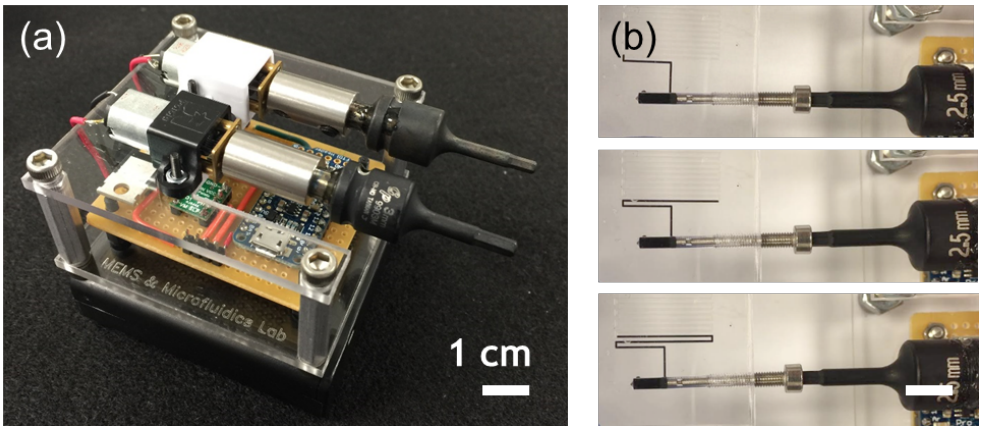

Figure 5.2. (a) Microcontroller-based screw pump for two DC motors. Two micro DC motors were mounted at the top layer, connected to the hex key driver via coupler. On the bottom layer, a microcontroller and two H-bridge circuits were interfaced on a circuit board. (b) Screw pump-actuated flow in microchannel using the Viton ball and rod configuration.

displacements of 2.0 μL and 2.8 μL per screw revolution are expected for the M3×0.5 and M4×0.7 screws, respectively. A maximum flow rate of 18.1 μL/min was achieved for the M3 screw at 100% duty cycle, while the larger thread pitch M4 screw yielded a maximum flow rate of 37.3 μL/min. A video montage showing microchannel flow over a range of applied motor duty cycles for the case of an M4 screw pump is provided as electronic supplemental information.

The higher friction associated with the larger screw resulted in increased flow rate variations compared with the M3 screws, with RSD as high as 14% at low duty cycles. Ultimately, friction limited the smallest achievable duty cycle, and thus the lowest flow rate, for both the M3 and M4 screw pumps. For the case of the M4 screw, a minimum flow rate of 1.45 μL/min was realized at 5.1% duty cycle, while the lower friction of the M3 screw device enabled a minimum flow rate of 0.43 μL/min at 3.5% duty cycle. Ultimately, the dynamic range of the screw-enabled pumps depends on motor performance, with the motors selected in this work reflecting a particular balance between cost, size, torque, and speed.

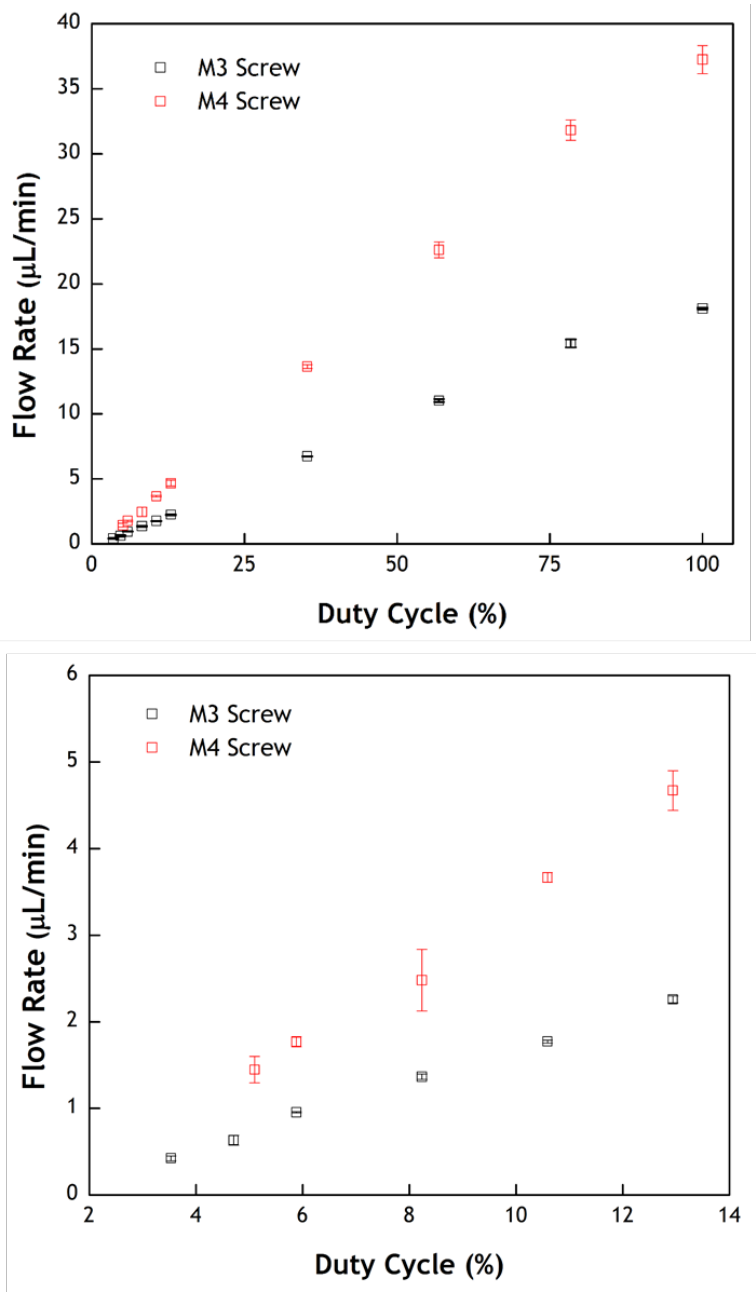

Figure 5.3. Flow rate of the screw-driven pump using Viton ball and rod configuration. (Top) Flow rate measured in full duty cycle range, and (bottom) finer measurement at low duty cycle. Using this configuration, flow rate can be tuned from 426 nL/min to over 18 µL/min. Error bars are ± 1 standard deviation.

In conventional syringe pumps which commonly employ stepper motors for precise actuation, unwanted pulsatile flow can often be observed at low flow rates due to periodic action of the motor driving the syringe plunger. Because the integrated syringe pumps described here employ PWM signals for motor actuation, with a PWM base frequency of approximately 500 Hz, pulsatile flow at this same frequency is expected. Because this frequency is well above the frame rate used for video capture, however, no pulsatile flow was observed in our experiments. Furthermore, any compliance within the fluidic system serves to reject high frequency disturbances in the flow, with higher levels of smoothing occurring at higher input frequencies. Thus the integrated pumps can offer enhanced flow uniformity compared with standard off-chip syringe pumps, although at the cost of reduced flow rate precision afforded by the use of stepper motors.

5.4.3. Pump Sealing

In the previous tests, a small amount of liquid was often observed to leak past the screw threads and exit the chip at higher flow rates. Characterization of the leakage pressure revealed that back pressures above approximately 100 kPa were sufficient to result in significant and routine fluid leakage for both M3 and M4 screws. In conventional syringe pumps, an elastomer seal attached to the tip of the syringe plunger serves to prevent leakage during actuation. Following a similar approach for sealing in the integrated screw pumps, we first sought to address the leakage issue by fabricating stainless steel rods equipped with circumferential grooves to house miniature O-rings (Figure 5.4(a)). Each rod was designed to serve as a sealed plunger which can move within the smoothbored reservoir port. Following established design guidelines,[155] O-

ring dimensions were chosen such that a 30% compressive strain and 9% stretching strain is induced when the O-ring is placed in the grooved section of the rod. Using this design, the resulting O-ring seals were found to prevent pump leakage at a maximum pressure of 0.7 ± 0.2 MPa, demonstrating their utility for low-pressure pumping. However, manual insertion of the miniature plunger into the screw reservoir often resulted in the O-ring dislodging from the shaft groove, necessitating multiple insertion attempts and damage to the sealing surfaces. More fundamentally, higher pumping pressures than those provided by the O-ring seal are commonly needed for many microfluidic applications. To increase the pressure limits while eliminating the chance of seal failure during plunger insertion, the O-ring was replaced with a simple fluoropolymer elastomer ball with a diameter slightly larger than that of the solvent-polished reservoir barrel. After testing several size differences ranging from 1% to 13%, elastomer balls 5% larger than the reservoir diameter were chosen to provide effective sealing without introducing excessive friction in the system. An SEM image of an elastomer ball partially inserted into a reservoir is shown in Figure 5.4(b). When using this configuration to characterize leakage pressure for the elastomer ball seals,

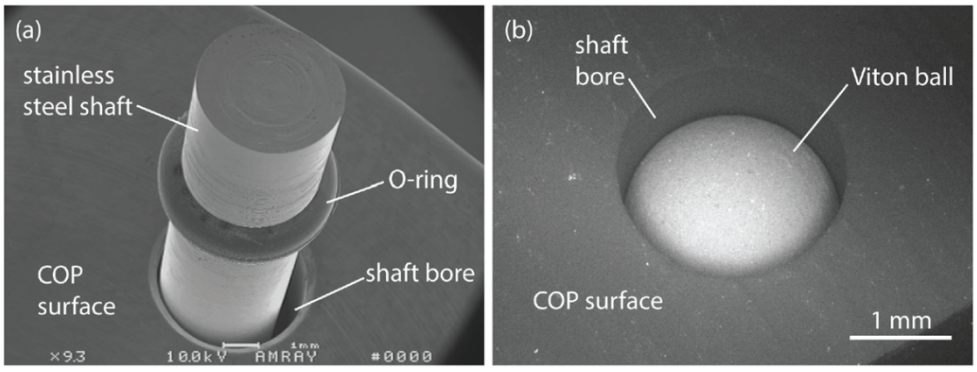

Figure 5.4. (a) O-ring integrated with a machined stainless steel rod and (b) polymer ball inserted into the solvent-polished reservoir of a fabricated screw pump chip.

tested devices failed due to delamination of the bonding interface between microchannel and reservoir substrates, rather than leakage past the seal. In these tests, an average sealing pressure of 4.7 ± 1.7 MPa was measured. No seal leakage was observed even at the maximum recorded pressure of 6.6 MPa, confirming that the fluoropolymer elastomer balls serve as an excellent high pressure seal for the on-chip screw pumps.

The use of solvent polishing to smooth the machined reservoir walls was found to be critical in enhancing device sealing when employing both the elastomer O-rings and balls. Without solvent polishing, damage to the Viton components was often observed following actuation, together with Viton residue and small amounts of fluid on the reservoir walls indicating an incomplete seal. Neither issue was observed for any of the solvent polished devices explored in this work.

5.4.4. Burst Valve Integration

To support on-chip packaging of reagents for integrated assays, sealing of liquids within the microfluidic chips is necessary. Sealing is required to prevent fluid loss by evaporation, to avoid potential user exposure to toxic or biologically active materials, and to minimize the potential for external contamination of the on-chip reagents. The screw pump seals serve this function on the inlet side of the pump reservoirs, but downstream sealing is also required to isolate fluids within the on-chip reservoirs. To demonstrate that fluids may be fully sealed within a thermoplastic chip prior to pumping, integrated screw pumps with elastomer ball seals were combined with single-use burst valves. The burst valves are fabricated using an established

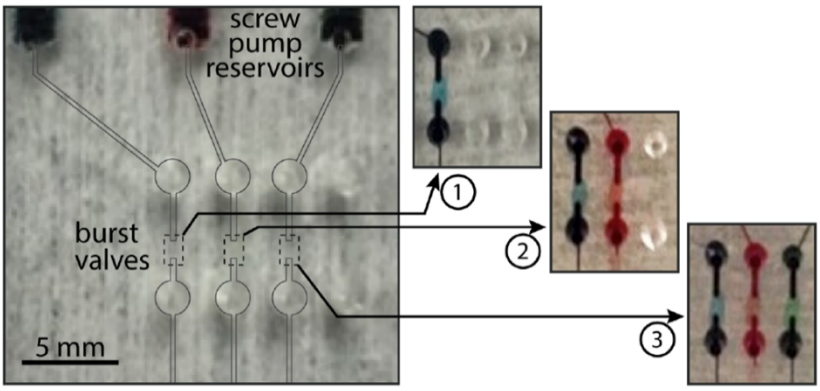

Figure 5.5. Fabricated chip containing 3 screw pumps with dye/water solutions stored in the screw pump reservoirs, and connected to single-use burst valves for hermetic sealing. Sequential independent actuation of each pump and burst valve is demonstrated in the inset images.

process.[154] Briefly, each valve region was defined by selective oxidation exposure to UV/ozone through a mask, followed by solvent swelling of the unexposed regions to raise the surface by several micrometers to form small gaps at the valves, followed by thermal bonding to temporarily close the gaps, thereby sealing the valves with a weak bond that may be reversed by application a burst pressure of approximately 1.5 MPa, well within the pressure limits of the integrated pumps. A microfluidic device containing 3 independent sets of screw pumps, burst valves, and reagent reservoirs was fabricated, as shown in Figure 5.5. In this device, the downstream channels connect to a single outlet channel routed to a shared waste reservoir. Before testing burst valve actuation, effective sealing of the storage chambers was verified by applying vacuum at the reservoir and monitoring motion of liquid past the valve. While hermeticity of the screw pump seal was not directly tested, we note that for applications where hermeticity is important, reagents may be stored between a pair of on-chip burst valves coupled to the pump inlet, obviating the need for a truly hermetic seal at the pump itself. For the device shown in Figure 5.5, each screw pump was operated in sequence

at a flow rate of approximately 10 μL/min, resulting in rapid buildup of pressure and opening the connected valve within 1 s following initial pump actuation. Independent valve opening was achieved in each of the channels, with no crosstalk between the fluidically-coupled valves observed. This demonstration confirms that the combination of sealed screw pumps and burst valves represents an effective method for on-chip storage and on-demand delivery of liquid reagents within thermoplastic microfluidic systems.

5.4.5. Two-Phase Droplet Generation

To further evaluate performance of the integrated screw pumps, a microfluidic two-phase water-in-oil droplet generator was fabricated with independent pumps for storage and delivery of each phase. All device inlet channels were 150 μm wide, with a droplet pinching region initially 88 μm wide and expanding to 150 μm. The height of all channels was 60 μm. A solution of dye in water with 1 wt% TWEEN 20 surfactant was added to the central reservoir during pump assembly, while silicone oil was added to the outer reservoirs coupled to the sheath flow microchannels. To maximize the achievable range of flow rate ratios between the two phases, the aqueous phase pump utilized an M3 screw while the two oil phase pumps were fabricated with M4 screws.

To obtain uniform droplets, microchannel droplet generation requires precise flow rate control as well as a stable infusion for both the continuous and dispersed phases. The size of droplet was tuned by varying duty cycle the motors to achieve different flow rate ratios, with droplets monitored under an optical microscope. In our tests, the duty cycle of oil phase M4 screw was varied between 8.2% and 17.7%, while

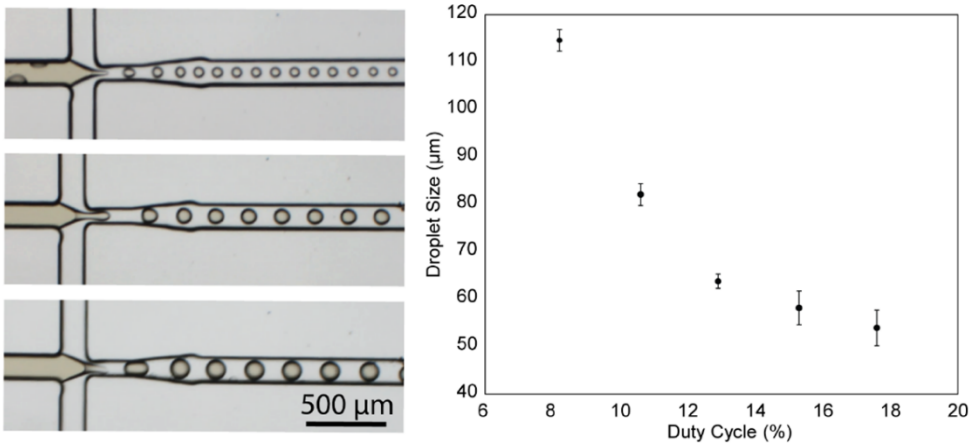

Figure 5.6. Droplet generation performed on two-motor system with Viton ball configuration. Dispersed phase reservoir was tapped for M3 screw then fixed at 5.9% duty cycle. Continuous phase reservoir was tapped for M4 screw, then duty cycle was varied from 8.2% to 17.7%. Three images are corresponding to 8.2%, 10.6%, and 17.7%, respectively.

holding the aqueous phase M3 screw duty cycle at 5.9%. As shown in Figure 5.6, stable droplets with excellent size uniformity were generated under these conditions, with droplet diameters ranging from 54.0 ± 3.8 µm to 114.6 ± 2.3 µm.

5.5. Conclusion

The integration of micropumps into thermoplastic microfluidic systems enabling on-chip reagent storage is needed to overcome limitations associated with world-to-chip fluidic interfacing in these systems. The screw-actuated displacement micropumps described in this work present new opportunities for the development of disposable assays using thermoplastic microfluidics. The ability to integrate on-chip screws as low cost functional pumping elements, while isolating higher cost reusable components including motors and control circuitry in a self-contained and compact form factor separate from the microfluidic device, makes the technology well suited to the development of microfluidic assays for use in small clinical settings or for portable

operation. Because software-defined flow profiles may be readily established using the demonstrated platform, with precise control over reagent flow rates from multiple on-chip reservoirs, the screw-enabled pumps can be used to manipulate complex fluidic operations limited only be the number of motors that may be positioned around the chip periphery. Finally, we note that actuation of the on-chip screws may also be performed manually, *e.g.* using a handheld driver rather than servo motors, for applications where it is desirable to minimize system cost and complexity, or where reliance on batteries to power the motors is not ideal.

Chapter 6: Conclusion

6.1. Summary

In this dissertation, we explored various microfluidic size-based separation techniques with the objective of developing rapid, efficient, and simple clinical sample preparation system for rapid detection of bacterial infection. Microfluidic techniques demonstrated here offered a compact, portable, and easy-to-operate solutions for sample preparation as well as various approaches to integrate microfluidic functions to maximize its efficiency even at a remote setting, or resource-poor environment.

In the aim of developing a sample preparation platform for bacterial detection in blood based on microfluidic techniques, a micro-porous silica monolith was employed as an essential component to trigger mechanical lysis of red blood cells. The simple principle of lysis not only offers a strong advantages over conventional passive microfluidic separation methods or chemical lysis approach, but also proved its versatility to process different gram types, size, and shape of bacteria on a same device at the same operation condition. However, mechanical lysis of a cell required a strong pressure-driven flow to push a cell into a pore, resulted in more frequent cell clogging for whole blood.

In the following two chapters, different hydrodynamic separation techniques were explored to improve the performance of monolith system by removing cell population at moderate level prior to the monolith device. A new innovative concept of hybridized clinical tool, named lab-on-a-syringe, was developed to enable pre-

processing of sample at the moment of blood draw. A unique thermoplastic solvent casting method not only enabled the microfabrication at a micron scale, but also offered an unconventional solution for three dimensional integration of thermoplastic microfluidic devices. The lab-on-a-syringe device showed how microfluidic designs could benefit from non-planar geometry, opening a new path toward the development of hybrid, multifunctional solutions using a conventional clinical tools such as disposable syringe. Apart from the lab-on-a-syringe, the miniaturized hydrocyclone was presented as another pre-processing device especially focused on throughput. Utilizing a 3D printing technique, a powerful separator commonly built in meter scale for the engineering plant was successfully miniaturized into a millimeter scale. μHC successfully showed particle separation at two orders of magnitude higher than the throughput of conventional microfluidic separation methods. Simple operation principle of pressure-driven flow expanded its potential toward instrumentation-free, portable sample preparation device and ultimately toward the POC clinical sample preparation.

At last, a strategy to truly realize the idea of lab-on-chip is discussed in the perspective of device operation and on-chip reagent storage. A miniaturized fluid actuator called “screw pump” and a thermoplastic device integrated with a reagent storage, microfluidic design, and simple fluidic interfacing are presented. The fluidic actuator capable of precise flow control over a wide range, various operation mode, and multiple actuation combined with a simple fluidic interfacing solution not only benefits the microfluidic devices presented in this dissertation, but also easily adaptable to the conventional thermoplastic microfluidic system. On-chip reagent storage idea

presented here was simple and low-cost but highly stable up to several megapascal pressure, and miniature fluid actuator was compact, and battery-powered, minimizing the need of sample loading step or bulky fluid actuator which binds the current LOC process to the laboratory.

6.2. Contribution to Field

The porous silica monolith offers an alternative approach to conventional size-exclusive techniques for blood specimen process. Unlike the conventional fibrous membrane or polymer-based porous element, porous silica monolith takes advantage of superior mechanical rigidity, enabling the mechanical lysis of cells at whole blood level. Facile scaling of the sol-gel chemistry greatly improves manufacturability of proposed device. In contrast to many size-based separation techniques which requires significant size differences between the target and the other component, precise fluidic control, or time-consuming process, simple flow-through operation through a porous silica monolith offers a simple solution that is applicable to various types of bacteria without any system modification.

Lab-on-a-syringe device demonstrated in this dissertation a new idea of smart tools for healthcare. The device utilized only a thermoplastic device and a common clinical tool to realize high quality micro structures in a cost-effective way compared to PDMS device or inorganic material. Unique thermoplastic soft lithography demonstrated a successful integration of microfluidic system onto a three-dimensional substrate, and it overcame the limitation of traditional thermoplastic fabrication methods which restricted to two-dimensional geometry. DLD lab-on-a-syringe device

took advantage of the shape of the substrate, and realized highly complex microfluidic system in an unconventional way.

Micro hydrocyclone realized via 3D printing technique reported the first successful hydrocyclone in a single millimeter scale. In spite of its superb throughput and separation efficiency, the extremely complex internal structure of hydrocyclone has been a major obstacle not only for advancing the theoretical understanding in miniaturized scale but also for optimizing its design, configuration, or operation parameters. The majority of study for small scale hydrocyclone is still focused on simulation side due to the difficulties of realizing the μHC structure, and the μHC presented the first experimental efforts toward the single micron scale separation within a millimeter scale hydrocyclone. In addition, the successful fabrication and following attempts to improve the separation performance through design modification provided good strategies toward the application of micro hydrocyclone in clinical fields.

Miniaturized fluid actuator with programmable controller, compact size coupled with highly stable reagent storage and simple interfacing methods presents a promising solution for various lab-on-a-chip diagnostics in a resource-limited setting, or in a time-sensitive situation. Programmable operator composed of cost-effective microprocessor combined with common DC motors demonstrated robust fluid manipulation, while easily multiplexed or replicated. Thermoplastic cassette-type device showed excellent sealing stability with a simple Viton ball, and enabled fluidic control at the level of hundreds nanoliters per minute by using a common screw. Combined system successfully demonstrated a complex fluidic operation, droplet

generation using two motors, which offers a strong potential of our portable miniature pump to replace the conventional syringe pump.

6.3. Future Work

6.3.1. Downstream Purification of Silica Monolith Processed Sample

The porous silica monolith was able to selectively lyse blood cells while isolating bacteria without losing viability. However, to enable rapid detection of bacteria from processed sample, the presence of cell lysate can cause significant disturbance during detection. According to our DLS analysis, mechanically lysed cell produces lysate at the scale of one hundred nanometers, which size is separated far enough from the size of typical bacteria found in blood stream infection. In addition, due to the low population of bacteria in blood compared to other components, concentrating the bacterial suspension is required to maximize the detection efficiency. A simple solution for this objective is to add a simple filter-equipped centrifugation tube with defined pore size. Gravitational acceleration will direct flow pass through the filter element, and objects larger than the membrane size will be retained in supernatant solution. Decreased indicator of blood cell membrane component in supernatant solution will ensure the improved quality of the processed sample from porous silica monolith with a simple addition to current system.

Bibliography

1 P. St-Louis, *Clin. Biochem.*, 2000, **33**, 427–440.

2 S. A. Soper, K. Brown, A. Ellington, B. Frazier, G. Garcia-Manero, V. Gau, S. I. Gutman, D. F. Hayes, B. Korte, J. L. Landers, D. Larson, F. Ligler, A. Majumdar, M. Mascini, D. Nolte, Z. Rosenzweig, J. Wang and D. Wilson, in *Biosensors and Bioelectronics*, 2006, vol. 21, pp. 1932–1942.

3 S. Sharma, J. Zapatero-Rodríguez, P. Estrela and R. O'Kennedy, *Biosensors*, 2015, 5, 577–601.

4 K. Hsieh, B. S. Ferguson, M. Eisenstein, K. W. Plaxco and H. T. Soh, *Acc. Chem. Res.*, 2015, **48**, 911–920.

5 A. Larsson, R. Greig-Pylypczuk and A. Huisman, *Ups. J. Med. Sci.*, 2015, 120, 1–10.

6 J. L. V. Shaw, *Pract. Lab. Med.*, 2016, **4**, 22–29.

7 J. Wang, *Electrochem. Sensors, Biosens. their Biomed. Appl.*, 2008, **108**, 57–69.

8 N. S. Oliver, C. Toumazou, A. E. G. Cass and D. G. Johnston, *Diabet. Med.*, 2009, **26**, 197–210.

9 Y. Hwa, D. Soo, Y. Na, H. Kim, D. Ho, S. Ahn, J. Yang, W. Seok and S. Seo, *Biosens. Bioelectron.*, 2012, **37**, 82–87.

10 B. C. Towe and V. B. Pizziconi, *Biosens. Bioelectron.*, 1997, **12**, 893–899.

11 J. R. L. Ehrenkranz, in *Epidemiology*, 2002, vol. 13.

12 T. Chard, *Hum. Reprod.*, 1992, **7**, 701–710.

13 G. A. Posthuma-Trumpie, J. Korf and A. van Amerongen, *Anal. Bioanal.*

Chem., 2009, **393**, 569–582.

14 H. Li, D. Han, G. M. Pauletti and A. J. Steckl, *Lab Chip*, 2014, **14**, 4035–4041.

15 D. H. Choi, S. K. Lee, Y. K. Oh, B. W. Bae, S. D. Lee, S. Kim, Y.-B. Shin and M.-G. Kim, *Biosens. Bioelectron.*, 2010, **25**, 1999–2002.

16 J. Zhu, N. Zou, D. Zhu, J. Wang, Q. Jin, J. Zhao and H. Mao, *Clin. Chem.*, 2011, **57**, 1732–1738.

17 A. T. Woolley, D. Hadley, P. Landre, A. J. DeMello, R. A. Mathies and M. A. Northrup, *Anal. Chem.*, 1996, **68**, 4081–4086.

18 M. V. Riquelme, H. Zhao, V. Srinivasaraghavan, A. Pruden, P. Vikesland and M. Agah, *Sens. Bio-Sensing Res.*, 2016, **8**, 47–54.

19 J.-G. Guan, Y.-Q. Miao and Q.-J. Zhang, *J. Biosci. Bioeng.*, 2004, **97**, 219–226.

20 M. S. Wiederoder, I. Misri and D. L. DeVoe, *Sensors Actuators, B Chem.*, 2016, **234**, 493–497.

21 J.-Y. Chen, Y.-T. Huang, H.-H. Chou, C.-P. Wang and C.-F. Chen, *Lab Chip*, 2015, **15**, 4533–4541.

22 W. Dungchai, O. Chailapakul and C. S. Henry, *Anal. Chim. Acta*, 2010, **674**, 227–233.

23 F. R. De Souza, G. L. Alves and W. K. T. Coltro, *Anal. Chem.*, 2012, **84**, 9002–9007.

24 M. J. Espy, J. R. Uhl, L. M. Sloan, S. P. Buckwalter, M. F. Jones, E. A. Vetter, J. D. C. Yao, N. L. Wengenack, J. E. Rosenblatt, F. R. Cockerill and T. F. Smith, *Clin. Microbiol. Rev.*, 2006, **19**, 165–256.

25 S. Pahlow, S. Meisel, D. Cialla-May, K. Weber, P. Rösch and J. Popp, *Adv. Drug Deliv. Rev.*, 2015, **89**, 105–120.

26 A. Manz, H. M. Widmers and N. Graber, *Sensors Actuators B Chem.*, 1990, **1**, 244–248.

27 D. R. Reyes, D. Iossifidis, P. A. Auroux and A. Manz, *Anal. Chem.*, 2002, **74**, 2623–2636.

28 H. A. Stone, A. D. Stroock and A. Ajdari, *Annu. Rev. Fluid Mech.*, 2004, **36**, 381–411.

29 G. M. Whitesides, *Nature*, 2006, **442**, 368.

30 P. Abgrall and A. M. Gué, *J. Micromechanics Microengineering*, 2007, **17**, R15–R49.

31 A. J. Mach and D. di Carlo, *Biotechnol. Bioeng.*, 2010, **107**, 302–311.

32 Z. Wu, B. Willing, J. Bjerketorp, J. K. Jansson and K. Hjort, *Lab Chip*, 2009, **9**, 1193.

33 H. W. Hou, R. P. Bhattacharyya, D. T. Hung and J. Han, *Lab Chip*, 2015, **15**, 2297–2307.

34 J. J. Lee, K. J. Jeong, M. Hashimoto, A. H. Kwon, A. Rwei, S. A. Shankarappa, J. H. Tsui and D. S. Kohane, *Nano Lett.*, 2014, **14**, 1–5.

35 J. H. Kang, M. Super, C. W. Yung, R. M. Cooper, K. Domansky, A. R. Graveline, T. Mammoto, J. B. Berthet, H. Tobin, M. J. Cartwright, A. L. Watters, M. Rottman, A. Waterhouse, A. Mammoto, N. Gamini, M. J. Rodas, A. Kole, A. Jiang, T. M. Valentin, A. Diaz, K. Takahashi and D. E. Ingber, *Nat. Med.*, 2014, **20**, 1211–1216.

36 B. G. J. M., *Electrophoresis*, 2000, **21**, 3931–3951.

37 J. D. Ramsey and G. E. Collins, *Anal. Chem.*, 2005, **77**, 6664–6670.

38 P. Sajeesh and A. K. Sen, *Microfluid. Nanofluidics*, 2014, **17**, 1–52.

39 D. Di Carlo, J. F. Edd, K. J. Humphry, H. A. Stone and M. Toner, *Phys. Rev. Lett.*, 2009, **102**, 94503.

40 J. Zhang, S. Yan, D. Yuan, G. Alici, N.-T. Nguyen, M. Ebrahimi Warkiani and W. Li, *Lab Chip*, 2016, **16**, 10–34.

41 J. Zhou and I. Papautsky, *Lab Chip*, 2013, **13**, 1121.

42 D. Di Carlo, *Lab Chip*, 2009, **9**, 3038.

43 H. Amini, W. Lee and D. Di Carlo, *Lab Chip*, 2014, **14**, 2739.

44 D. W. Inglis, J. A. Davis, R. H. Austin and J. C. Sturm, *Lab Chip*, 2006, **6**, 655.

45 L. R. Huang, E. C. Cox, R. H. Austin and J. C. Sturm, *Science (80-.).*, 2004, **304**, 987–990.

46 S. H. Holm, J. P. Beech, M. P. Barrett and J. O. Tegenfeldt, *Lab Chip*, 2011, **11**, 1326.

47 E. S. Asmolov, *Phys. Fluids*, 2002, **14**, 15–28.

48 E. S. ASMOLOV, *J. Fluid Mech.*, 1999, **381**, S0022112098003474.

49 J. P. Matas, J. F. Morris and É. Guazzelli, *J. Fluid Mech.*, 2004, **515**, 171–195.

50 D. Di Carlo, J. F. Edd, D. Irimia, R. G. Tompkins and M. Toner, *Anal. Chem.*, 2008, **80**, 2204–2211.

51 T. Morijiri, S. Sunahiro, M. Senaha, M. Yamada and M. Seki, *Microfluid. Nanofluidics*, 2011, **11**, 105–110.

52 M. Yamada, M. Nakashima and M. Seki, *Anal. Chem.*, 2004, **76**, 5465–5471.

53 M. Pødenphant, N. Ashley, K. Koprowska, K. U. Mir, M. Zalkovskij, B. Bilenberg, W. Bodmer, A. Kristensen and R. Marie, *Lab Chip*, 2015, **15**, 4598–4606.

54 Y. Xia and G. M. Whitesides, *Annu. Rev. Mater. Sci.*, 1998, **28**, 153–184.

55 C. W. Tsao and D. L. DeVoe, *Microfluid. Nanofluidics*, 2009, 6, 1–16.

56 H. Sharma, D. Nguyen, A. Chen, V. Lew and M. Khine, *Ann. Biomed. Eng.*, 2011, **39**, 1313–1327.

57 T. J. A. Renckens, D. Janeliunas, H. van Vliet, J. H. van Esch, G. Mul and M. T. Kreutzer, *Lab Chip*, 2011, **11**, 2035.

58 C. W. Tsao and D. L. DeVoe, *Microfluid. Nanofluidics*, 2009, **6**, 1–16.

59 A. Piruska, I. Nikcevic, S. H. Lee, C. Ahn, W. R. Heineman, P. A. Limbach and C. J. Seliskar, *Lab Chip*, 2005, **5**, 1348.

60 J. Y. Han, O. D. Rahmanian, E. L. Kendall, N. Fleming and D. L. DeVoe, *Lab Chip*, 2016, **16**, 3940–3946.

61 F. C. Tenover, *Clin. Infect. Dis.*, 2011, **52**, S338-45.

62 A. Kumar, D. Roberts, K. E. Wood, B. Light, J. E. Parrillo, S. Sharma, R. Suppes, D. Feinstein, S. Zanotti, L. Taiberg, D. Gurka, A. Kumar and M. Cheang, *Crit. Care Med.*, 2006, **34**, 1589–1596.

63 G. S. Martin, *Expert Rev. Anti. Infect. Ther.*, 2012, **10**, 701–706.

64 A. Van Belkum, G. Durand, M. Peyret, S. Chatellier, G. Zambardi, J. Schrenzel, D. Shortridge, A. Engelhardt and W. M. Dunne, *Ann. Lab. Med.*, 2013, **33**, 14–27.

65 V. Schmidt, A. Jarosch, P. März, C. Sander, V. Vacata and W. Kalka-Moll, *Eur. J. Clin. Microbiol. Infect. Dis.*, 2012, **31**, 311–317.

66 A. Bosch, A. Miñán, C. Vescina, J. Degrossi, B. Gatti, P. Montanaro, M. Messina, M. Franco, C. Vay, J. Schmitt, D. Naumann and O. Yantorno, *J. Clin. Microbiol.*, 2008, **46**, 2535–2546.

67 C. Sandt, C. Madoulet, A. Kohler, P. Allouch, C. De Champs, M. Manfait and G. D. Sockalingum, *J. Appl. Microbiol.*, 2006, **101**, 785–797.

68 U. Sharaha, E. Rodriguez-Diaz, K. Riesenberg, I. J. Bigio, M. Huleihel and A. Salman, *Anal. Chem.*, 2017, **89**, 8782–8790.

69 N. Xia, T. P. Hunt, B. T. Mayers, E. Alsberg, G. M. Whitesides, R. M. Westervelt and D. E. Ingber, *Biomed. Microdevices*, 2006, **8**, 299–308.

70 B. V. Bronk, W. P. Van De Merwe and M. Stanley, *Cytometry*, 1992, **13**, 155–162.

71 S. Zelenin, J. Hansson, S. Ardabili, H. Ramachandraiah, H. Brismar and A. Russom, *Biotechnol. Lett.*, 2015, **37**, 825–830.

72 N. Tanaka, H. Kobayashi, K. Nakanishi, H. Minakuchi and N. Ishizuka, *Anal. Chem.*, 2001, **73**, 420 A-429 A.

73 T. J. Silhavy, D. Kahne and S. Walker, *Cold Spring Harb. Perspect. Biol.*, , DOI:10.1101/cshperspect.a000414.

74 M. S. Islam, A. Aryasomayajula and P. R. Selvaganapathy, *Micromachines*, 2017, 8.

75 M. Mahalanabis, H. Al-Muayad, M. D. Kulinski, D. Altman and C. M. Klapperich, *Lab Chip*, 2009, **9**, 2811.

76 J. Liu, I. White and D. L. DeVoe, *Anal. Chem.*, 2011, **83**, 2119–2124.

77 J. Liu, C. F. Chen, C. W. Chang and D. L. DeVoe, *Biosens. Bioelectron.*, 2010, **26**, 182–188.

78 T. Hara, S. Makino, Y. Watanabe, T. Ikegami, K. Cabrera, B. Smarsly and N. Tanaka, *J. Chromatogr. A*, 2010, **1217**, 89–98.

79 M. Motokawa, H. Kobayashi, N. Ishizuka, H. Minakuchi, K. Nakanishi, H. Jinnai, K. Hosoya, T. Ikegami and N. Tanaka, *J. Chromatogr. A*, 2002, **961**, 53–63.

80 D. S. Peterson, T. Rohr, F. Svec and J. M. J. Fréchet, *Anal. Chem.*, 2002, **74**, 4081–4088.

81 J. Liu, C. F. Chen, C. W. Tsao, C. C. Chang, C. C. Chu and D. L. DeVoe, *Anal. Chem.*, 2009, **81**, 2545–2554.

82 O. Núñez, K. Nakanishi and N. Tanaka, *J. Chromatogr. A*, 2008, 1191, 231–252.

83 K. Kajihara, *J. Asian Ceram. Soc.*, 2013, **1**, 121–133.

84 H. Dong, M. A. Brook and J. D. Brennan, *Chem. Mater.*, 2005, **17**, 2807–2816.

85 G. Guiochon, *J. Chromatogr. A*, 2007, **1168**, 101–168.

86 M. Vázquez and B. Paull, *Anal. Chim. Acta*, 2010, **668**, 100–113.

87 M. He, J. Bin Bao, Y. Zeng and D. J. Harrison, *Electrophoresis*, 2010, **31**, 2422–2428.

88 E. L. Kendall, E. Wienhold, O. D. Rahmanian and D. L. Devoe, *Sensors Actuators, B Chem.*, 2014, **202**, 866–872.

89 E. L. Kendall, J. Y. Han, M. S. Wiederoder, A. Sposito, A. Wilson, O. D.

Rahmanian and D. L. DeVoe, *J. Polym. Sci. Part B Polym. Phys.*, 2015, **53**, 1315–1323.

90 S. R. Lockhart, M. A. Abramson, S. E. Beekmann, G. Gallagher, S. Riedel, D. J. Diekema, J. P. Quinn and G. V. Doern, *J. Clin. Microbiol.*, 2007, **45**, 3352–3359.

91 M. B. Edmond, S. E. Wallace, D. K. McClish, M. A. Pfaller, R. N. Jones and R. P. Wenzel, *Clin. Infect. Dis.*, 1999, **29**, 239–244.

92 E. A. Evans and R. Waugh, *Biophys. J.*, 1977, **20**, 307–313.

93 G. Tomaiuolo, *Biomicrofluidics*, 2014, **8**, 51501.

94 G. Tomaiuolo, M. Simeone, V. Martinelli, B. Rotoli and S. Guido, *Soft Matter*, 2009, **5**, 3736.

95 J. Dupire, M. Socol and A. Viallat, *Proc. Natl. Acad. Sci.*, 2012, **109**, 20808–20813.

96 E. A. Evans, R. Waugh and L. Melnik, *Biophys. J.*, 1976, **16**, 585–595.

97 T. Savin, M. M. Bandi and L. Mahadevan, *Soft Matter*, 2016, **12**, 562–573.

98 R. M. Hochmuth, *J. Biomech.*, 2000, **33**, 15–22.

99 M. Steinitz, *Anal. Biochem.*, 2000, **282**, 232–238.

100 H. Becker and C. Gärtner, *Anal. Bioanal. Chem.*, 2008, 390, 89–111.

101 S. H. Ng and Z. F. Wang, in *Microsystem Technologies*, 2009, vol. 15, pp. 1149–1156.

102 H. Lin, W. Peng, M. Zhang, J. Chen, H. Hong and Y. Zhang, *Desalination*, 2013, 314, 169–188.

103 S. O. Majekodunmi, *Am. J. Biomed. Eng.*, 2015, **5**, 67–78.

104 M. G. Lee, J. H. Shin, C. Y. Bae, S. Choi and J. K. Park, *Anal. Chem.*, 2013, **85**, 6213–6218.

105 D. M. Dohan Ehrenfest, N. R. Pinto, A. Pereda, P. Jiménez, M. Del Corso, B. S. Kang, M. Nally, N. Lanata, H. L. Wang and M. Quirynen, *Platelets*, 2017, 1–14.

106 J. H. Vogel and K. H. Kroner, *Biotechnol. Bioeng.*, 1999, **63**, 663–674.

107 S. Pasquier and J. J. Cilliers, *Chem. Eng. J.*, 2000, **80**, 283–288.

108 S. T. L. Harrison and J. J. Cilliers, *Miner. Eng.*, 1997, **10**, 529–535.

109 Z. Bai, H. Wang and S.-T. Tu, *Sep. Sci. Technol.*, 2009, **44**, 2067–2077.

110 C. Puprasert, G. Hebrard, L. Lopez and Y. Aurelle, *Chem. Eng. Process. Process Intensif.*, 2004, **43**, 67–83.

111 J. J. Cilliers, L. Diaz-Anadon and F. S. Wee, *Miner. Eng.*, 2004, **17**, 591–597.

112 D. Bradley, 1965.

113 K. Rietema, *Chem. Eng. Sci.*, 1961, **15**, 320–325.

114 L. R. Castilho and R. A. Medronho, *Miner. Eng.*, 2000, **13**, 183–191.

115 H. Gong, B. P. Bickham, A. T. Woolley and G. P. Nordin, *Lab Chip*, , DOI:10.1039/C7LC00644F.

116 H. Gong, M. Beauchamp, S. Perry, A. T. Woolley and G. P. Nordin, *RSC Adv.*, 2015, **5**, 106621–106632.

117 P. Bagdi, P. Bhardwaj and A. K. Sen, *J. Fluids Eng.*, 2012, **134**, 21105.

118 M. Shakeel Syed, M. Rafeie, R. Henderson, D. Vandamme, M. Asadnia and M. Ebrahimi Warkiani, *Lab Chip*, 2017, **17**, 2459–2469.

119 Z. S. Bai, H. L. Wang and S. T. Tu, *Pet. Sci. Technol.*, 2010, **28**, 525–533.

120 M. Ghadirian, A. Afacan, R. E. Hayes, J. P. Mmbaga, T. Mahmood, Z. Xu and J. Masliyah, *Can. J. Chem. Eng.*, 2015, **93**, 1667–1677.

121 D. R. . Mailapalli, P. A. A. Marques and K. J. Thomas, *Eng. Agrícola*, 2007, **27**, 373–382.

122 P. Bhardwaj, P. Bagdi and A. K. Sen, *Lab Chip*, 2011, **11**, 4012.

123 J. M. Pearce, *Open-Source Lab: How to Build Your Own Hardware and Reduce Research Costs*, 2013.

124 B. Wijnen, E. J. Hunt, G. C. Anzalone and J. M. Pearce, *PLoS One*, 2014, **9**, 1–8.

125 E. Gibney, *Nature*, 2016, 531, 147–148.

126 Y. Temiz, R. D. Lovchik, G. V. Kaigala and E. Delamarche, *Microelectron. Eng.*, 2015, **132**, 156–175.

127 Y. X. Guan, Z. R. Xu, J. Dai and Z. L. Fang, *Talanta*, 2006, **68**, 1384–1389.

128 L. Gervais, M. Hitzbleck and E. Delamarche, *Biosens. Bioelectron.*, 2011, **27**, 64–70.

129 L. Gervais and E. Delamarche, *Lab Chip*, 2009, **9**, 3330.

130 F. Lu, Q. Mao, R. Wu, S. Zhang, J. Du and J. Lv, *Lab Chip*, 2015, **15**, 495–503.

131 M. Zimmermann, P. Hunziker and E. Delamarche, *Microfluid. Nanofluidics*, 2008, **5**, 395–402.

132 W. Bin Du, Q. Fang, Q. H. He and Z. L. Fang, *Anal. Chem.*, 2005, **77**, 1330–1337.

133 N.-T. Nguyen, X. Huang and T. K. Chuan, *J. Fluids Eng.*, 2002, **124**, 384.

134 F. Abhari, H. Jaafar and N. A. Md Yunus, *Int. J. Electrochem. Sci.*, 2012, **7**, 9765–9780.

135 A. Nisar, N. Afzulpurkar, B. Mahaisavariya and A. Tuantranont, *Sensors Actuators B Chem.*, 2008, **In Press,** 917–942.

136 C. Zhang, D. Xing and Y. Li, *Biotechnol. Adv.*, 2007, **25**, 483–514.

137 G. Li, Y. Luo, Q. Chen, L. Liao and J. Zhao, *Biomicrofluidics*, , DOI:10.1063/1.3692770.

138 D. B. Weibel, A. C. Siegel, A. Lee, A. H. George and G. M. Whitesides, *Lab Chip*, 2007, **7**, 1832.

139 L. Xu, H. Lee and K. W. Oh, *Microfluid. Nanofluidics*, 2014, **17**, 745–750.

140 S. Elizabeth Hulme, S. S. Shevkoplyas and G. M. Whitesides, *Lab Chip*, 2009, **9**, 79–86.

141 D. B. Weibel, M. Kruithof, S. Potenta, S. K. Sia, A. Lee and G. M. Whitesides, *Anal. Chem.*, 2005, **77**, 4726–4733.

142 M. Rhee and M. A. Burns, *Lab Chip*, 2009, **9**, 3131.

143 I. K. Dimov, L. Basabe-Desmonts, J. L. Garcia-Cordero, B. M. Ross, A. J. Ricco and L. P. Lee, *Lab Chip*, 2011, **11**, 845–850.

144 W. Li, T. Chen, Z. Chen, P. Fei, Z. Yu, Y. Pang and Y. Huang, *Lab Chip*, 2012, **12**, 1587.

145 K. Iwai, K. C. Shih, X. Lin, T. A. Brubaker, R. D. Sochol and L. Lin, *Lab Chip*, 2014, **14**, 3790.

146 H. Lai and A. Folch, *Lab Chip*, 2011, **11**, 336–342.

147 C.-Y. Chen, C.-H. Chen, T.-Y. Tu, C.-M. Lin and A. M. Wo, *Lab Chip*, 2011,

11, 733–737.

148 P. Gu, K. Liu, H. Chen, T. Nishida and Z. H. Fan, *Anal. Chem.*, 2011, **83**, 446–452.

149 D. A. Markov, S. Manuel, L. M. Shor, S. R. Opalenik, J. P. Wikswo and P. C. Samson, *Biomed. Microdevices*, 2010, **12**, 135–144.

150 M. Liong, A. N. Hoang, J. Chung, N. Gural, C. B. Ford, C. Min, R. R. Shah, R. Ahmad, M. Fernandez-Suarez, S. M. Fortune, M. Toner, H. Lee and R. Weissleder, *Nat. Commun.*, , DOI:10.1038/ncomms2745.

151 C.-F. Chen, J. Liu, C.-C. Chang and D. L. DeVoe, *Lab Chip*, 2009, **9**, 3511.

152 K. J. Cha and D. S. Kim, *Biomed. Microdevices*, 2011, **13**, 877–883.

153 M. M. Gong, B. D. MacDonald, T. Vu Nguyen and D. Sinton, *Biomicrofluidics*, , DOI:10.1063/1.4762851.

154 O. D. Rahmanian and D. L. DeVoe, *Microfluid. Nanofluidics*, 2015, **18**, 1045–1053.

155 P. Seals, *Parker O-Ring Handbook*, 2007.